Acidic Properties of Alkaline-Earth Phosphates Determined by an Experimental-Theoretical Approach

E. Blanco, Q. Gu, J. Couble, L. Martin, T. Onfroy, G. Costentin, Jean-Francois Paul, Carine Michel, S. Loridant

Acidic Properties of Alkaline-earth Phosphates Determined by an Experimental-Theoretical Approach

Journal:	*The Journal of Physical Chemistry*
Manuscript ID	jp-2019-10472y.R1
Manuscript Type:	Article
Date Submitted by the Author:	n/a
Complete List of Authors:	Blanco, Elodie; Institut de Recherches sur la Catalyse et l'Environnement de Lyon GU, Qingyi; Ecole normale superieure de Lyon Couble, Julien; Institut de Recherches sur la Catalyse et l'Environnement de Lyon Martin, Lucile; Unité de Catalyse et Chimie du Solide Onfroy, Thomas; UPMC, Laboratoire Systemes Interfaciaux Echelle Nanometrique Costentin, Guylene; UPMC, Lab. Réactivité de Surface Paul, Jean-François; Unité de Catalyse et Chimie du Solide Michel, Carine; Ecole normale superieure de Lyon, Laboratoire de Chimie Loridant, Stephane; Institut de Recherches sur la Catalyse et l'Environnement de Lyon

Acidic Properties of Alkaline-earth Phosphates Determined by an Experimental-Theoretical Approach

Elodie Blanco[a], Qingyi Gu[b], Julien Couble[a], Lucile Martin[c], Thomas Onfroy[d], Guylène Costentin[d], Jean-François Paul[c], Carine Michel[b,], Stéphane Loridant[a,*]*

[a] Univ Lyon, Université Claude Bernard-Lyon 1, CNRS, IRCELYON-UMR 5256, 2 av. A. Einstein, F-69626 Villeurbanne Cedex, France

[b] Univ Lyon, Ens de Lyon, CNRS UMR 5182, Université Claude Bernard Lyon 1, Laboratoire de Chimie, F69342, Lyon, France

[c] Univ. Lille, CNRS, Centrale Lille, ENSCL, Univ. Artois, UMR 8181-UCCS Unité de Catalyse et Chimie du Solide, F-59000 Lille, France

[d] Sorbonne Université, CNRS, Laboratoire Réactivité de Surface, LRSUPMC Univ Paris 06, UMR 7197, Laboratoire Réactivité de Surface, F-75005 Paris, France

ABSTRACT. Alkaline-earth phosphates efficient in the dehydration of lactic acid to acrylic acid were previously shown to contain a surface mono/dihydrogen phosphate amorphous layer composed by M^{2+} cations, P=O and POH groups. In this work, acidic properties of such a layer were determined combining FTIR spectra achieved at the dehydrated state and under water vapor and DFT simulations of non-defective and defective MPOH structure. The FTIR spectra of adsorbed pyridine and lutidine revealed the presence of moderate Lewis acid sites (LAS) and of POH groups interacting by H-bonding without significant protonation. DFT calculations were key to interpret FTIR spectra after adsorption of NH_3: when solely adsorbed, NH_3 interacts with the LAS on both the non-defective surface and the defective surface while the POH for which H points up towards the gas phase are reoriented downward. Brønsted acid sites (BAS) were shown to form under water vapor. This phenomenon was shown by DFT to arise from a more acidic character of HPO_4^{2-} species for non-defective surface and casual formation of non-defective surface leading to higher amount of $H_2PO_4^-$ species, which are more acidic BAS.

1. INTRODUCTION

Acrylic Acid (AA) is a platform molecule used as a building block to produce acrylate polymers and plastics and currently produced by catalytic oxidation of propylene in large volume (6 Mt/y predicted by 2020).[1,2] From both environmental and economical point of view, alternative routes to produce acrylic acid should be developed. Glycerol is a potential renewable raw material to produce acrylic acid by oxidehydration.[3] Yields higher than 50% were obtained on W-V-Nb mixed oxides with hexagonal tungsten bronze structure.[4,5]

Another investigated route is the dehydration of Lactic Acid (LA), a platform molecule used to produce chemical commodities and PLA polymers.[1,2,6] Lactic acid is currently yielded by carbohydrates fermentation[1,2,6] but can also be obtained by alternative fermentation processes using various substrates[7,8] and by glycerol catalytic dehydrogenation.[9] The global market for lactic acid was 0.75 Mt/y in 2017 and is projected to reach 1.8 Mt/y by 2022.[10] Modified zeolites, sulphates/nitrates, and phosphates were specifically investigated. The best yields were obtained using alkaline earth metal phosphates (up to 85% AA yield) which furthermore are more stable than zeolites.[1,2,6]

We established correlations between the NH_3 and CO_2-TPD curves and the AA selectivity using alkaline earth phosphates as catalysts.[11] The catalysts with only weak acid and basic sites were selective and their NH_3 and CO_2-TPD curves were surprisingly quite similar. Furthermore, the best AA selectivity was obtained for barium orthophosphate, for which the acid to base balance was close to 1. It suggested the participation of acid-base pairs in the mechanism. However, TPD measurements were achieved after pre-treatment at the calcination temperature while water vapor was present in the reaction feed and generated by dehydration. More recently, characterization of the prepared alkaline earth phosphates (including barium orthophosphate) showed the systematic

presence of a surface mono/dihydrogen phosphate amorphous (non-crystalline for X-rays and electron diffraction) layer containing POH species.[12] *In situ* DRIFT measurements have suggested that formation of POH groups was favored under water vapor and that these species interacted with reactants or reaction products at the reaction temperature.

DFT calculations could help in rationalizing the experimental observations. For instance, Paul and co-workers investigated the LA to AA transformation but on ZrO_2.[13] They identified that on this oxide, the dehydration site is clearly an acido-basic pair, where the acid site Zr^{4+} stabilizes the leaving α-OH and the basic O^{2-} site on zirconia plays the role of proton acceptor. Theoretical studies were also achieved on alkaline earth phosphates but mostly on hydroxyapatites $Ca_5(PO_4)_3(OH)$ due to their important using in biomaterials.[14]

In the present work, acidic sites of alkaline-earth phosphates catalysts were characterized by NH_3 adsorption followed by IR spectroscopy at the dehydrated state and in the presence of water vapor. The IR spectra were assigned from DFT calculations, which also explained acidic properties determined by NH_3 adsorption. Characterization of acidity was strengthened by adsorption of pyridine and lutidine followed by IR spectroscopy.

2. METHODS

2.1 Catalysts preparation

Barium orthophosphate (labelled BaOP) was prepared by mixing a solution of diammonium hydrogen phosphate $(NH_4)_2HPO_4$ (Aldrich, 99%) at 0.20 mol.L^{-1} for which the pH was previously adjusted to 9 adding NH_4OH (32%vol) and a solution of barium nitrate ($Ba(NO_3)_2$) (Aldrich, >99%) at 0.30 mol.L^{-1}. The latter one was added drop wise while maintaining constant the pH and stirring for 1 h. The precipitate was filtrated off, washed with deionized water, dried at 100 °C and

crushed before calcination under air flow at 600 °C for 6 h.

2.2 Catalysts characterizations

Analysis of the acidic properties of samples was performed by adsorption-desorption of pyridine and lutidine followed by infrared spectroscopy. Self-supported wafers were placed inside the IR cell and then outgassed under secondary vacuum at 350 °C for 2 h. In the following, the samples were contacted at room temperature with gaseous basic probe via a separate cell containing liquid pyridine or lutidine. The spectra were then recorded following desorption at increasing temperature with a Bruker Vector 22 spectrometer (resolution 2 cm^{-1}, 64 scans). The reported spectra were obtained after subtraction of the spectrum recorded before probe adsorption.

In situ DRIFT spectra were achieved with a Nicolet 6700 FTIR spectrometer (Thermo Scientific) equipped with Praying Mantis™ High Temperature Reaction Chamber (Harrick, model HVC-DRP-4). The CaF_2 windows used for the experiments were heated at 70-80 °C with external water system to avoid condensation. The effect of water was investigated by flowing 30%H_2O-He or 30%D_2O-He at 380 °C after pre-treatment at 380 °C for 30 min under He. Such high water partial pressure was obtained using a saturator heated at 70 °C. The background corresponded to the spectrum of dehydrated KBr.

In situ FTIR acidity measurements were performed on self-supported pellets (53 mg) with a Nicolet 6700 spectrometer (ThermoScientific) using a homemade stainless steel IR cell reactor specially designed to limit the gas phase contribution (its optical path is 2.2 mm)[15] and NH_3 as probe molecule. This IR cell allowed the study of adsorbed species in the range 20-450 °C under gas flow rates (200 $mL.min^{-1}$ in the present study) of gas mixtures at atmospheric pressure such as x% NH_3/y% H_2O/He with x and y in the ranges 0-1% and 0-3% respectively. The amount of H_2O

was controlled using a saturator/condenser system as described previously.[16] BaOP pellet was pre-treated at 380 °C under 20%O_2-He for 1 h and then He. NH_3 adsorption equilibrium was followed at 2%NH_3 upon heating and cooling between RT to 200 °C. The AEIR (Adsorption Equilibrium InfraRed spectroscopy) method was used to determine individual NH_3 heats of adsorption from the evolution of the IR band area of each adsorbed X_{ads} species with the increase in T_a in isobaric conditions. The experimental curve $\theta X_{exp} = f(T_a)$, with θ corresponding to the coverage of sites, was compared to the one obtained from the Temkin model assuming localized adsorbed species. Adjustment of the theoretical curve to the experimental data provides $E_x(1)$ and $E_x(0)$, the heats of adsorption at high and low coverages of the X_{ads} species, respectively. The accuracy of the method to determine NH_3 heats of adsorption has been evidenced for TiO_2 support and $V_2O_5/WO_3/TiO_2$ catalysts.[17-19] Acidity measurements in presence of water vapor[20] were achieved at adsorption equilibrium flowing 1%NH_3-3%H_2O-He mixture upon heating and cooling between RT and 200 °C.

2.3 DFT Computational details

Density functional theory (DFT) calculations were carried out using the Vienna ab initio simulation package (VASP).[21-23] The exchange and correlation terms were obtained by the Perdew–Burke–Ernzerhof form of Generalized Gradient Approximation (GGA-PBE) functional.[24] The core electrons were kept frozen and a projector-augmented wave (PAW) method was used to substitute the core electrons.[25] A cut-off energy of 550 eV of the plane wave basis set was used to describe the valence electrons. The bulk optimization would reach the convergence when the energy was converged to 1×10^{-6} eV and the forces were smaller than 0.01 eV/Å with a k-point mesh of 5×2×5. For optimization of the slab, the same energy convergence criterion was used and

the convergence criterium on the forces was set to 0.03 eV/Å. The k-point mesh was adapted to the super cell size using a mesh of 5×5×1 k-points. Frequencies were computed within the harmonic approximation. Gibbs free energies were derived using those frequencies, and for the molecules using the perfect gas and rigid rotator approximations.

Based on the previous characterizations of the BaOP catalyst[11,12] and on the fact that Ca and Ba are expected to have similar properties being both alkaline-earth elements, we selected the Brushite, a well-known layered calcium hydrogen orthophosphate dihydrate,[26-28] to model the amorphous layer lying over the catalyst crystallites. In solution, Brushite forms thin hexagonal platelet.[27,29] Since the (010) surface corresponds to the basal plane of the platelets, it is expected to be the most stable and have a very low surface energy. In order to define a model of this surface, the cutting plane was located in the middle of the gap between two layers. The number of water molecule was kept equal to the number in the solid. Using this choice, the surface is created cutting only hydrogen bonds. Two other planes perpendicular to the basal plane were studied: the (100) and the (001) in order to model the edges of the platelets. The two surfaces have been defined without breaking any P-O or O-H bonds, in order to reduce their surface energies. For the three surfaces, symmetric and stoichiometric slabs were used with a vacuum layer of 15.14 Å to avoid the interaction between the slabs. The computed surface energies for (001), (010) and (100) were 0.047 eV/Å^2, 0.016 eV/Å^2 and 0.032 eV/Å^2 respectively, confirming the greater stability of the (010) surface.

The adsorption of the molecules was performed on the top of the most favorable surface (010) surface using a p(2×2) asymmetric slab made of 16 $CaHPO_4 \cdot 2H_2O$, where the top surface layers, including 8 $CaHPO_4 \cdot 2H_2O$, were allowed to relax while the bottom 8 $CaHPO_4 \cdot 2H_2O$ were constrained during the geometry optimization.

The IR spectroscopy was modelled by accurately determining the vibrational spectrum of a system. We used the density functional perturbation theory in our study to determine the Hessian matrix, and finally obtain the wavenumber of every vibration mode.[30] Within this framework, the overtones are not simulated and the influence of the temperature on the vibration wavenumbers is not included. We determined the scaling factor between experimental wavenumbers and DFT ones using NH_3 and H_2O as a reference and we obtained 0.98 for the stretching vibration modes and 1.00 the for bending ones as shown in Table S1 of Supplementary material. Scaling down some wavenumbers to improve the quality of the prediction obtained within the harmonic approximation allows us to partially recover anharmonicity effects.[31-33] The good agreement with the experimental spectra confirms that this factor established on gas phase spectra of water and ammonia is still valid for adsorbed species.

3. RESULTS

3.1 Characterization of the dehydrated and hydrated state

The main structural and textural properties of BaOP catalyst have been previously described.[11] Shortly, it contained mostly crystalline $Ba_3(PO_4)_2$ and its specific surface area was 8.9 $m^2.g^{-1}$. Chemical and XPS analyses showed sub-stoichiometric Ba/P ratios (1.38 and 1.28, respectively instead of 1.5 for stoichiometric $Ba_3(PO_4)_2$) that could be ascribed to the presence of either small amount of crystalline α-$Ba_2P_2O_7$ [11] and a phosphorus rich amorphous (non-crystalline) phase which does not diffract either by X-rays and electron diffractions. The latter phase was shown to correspond to a surface layer containing POH species and lying over $Ba_3(PO_4)_2$ crystallites.[12] It could be either a stoichiometric $BaHPO_4$ or a mixture of mono and dihydrogen phosphate with a general formula $Ba_{(1-x)}(HPO_4)_{1-2x}(H_2PO_4)_{2x}$.

A DRIFT spectrum of BaOP treated under helium flow at 380 °C is plotted in Figure 1. The bands between 1850 and 2050 cm^{-1} corresponded to overtones of ν(P=O) vibrations which are located around 1000 cm^{-1}.[34] The band at 3660 cm^{-1} was ascribed to ν(PO-H) stretching vibrations of free surface species by analogy with deficient hydroxyapatites.[12] The broad band located around 3190 cm^{-1} corresponded to ν(PO-H) stretching vibrations as observed for alkaline earth hydrogen phosphates.[35-38] This large difference of wavenumber could arise from the effect of hydrogen bonds in bulk hydrogen phosphates leading to weakening of PO-H bonds and stretching vibrations at lower wavenumbers.

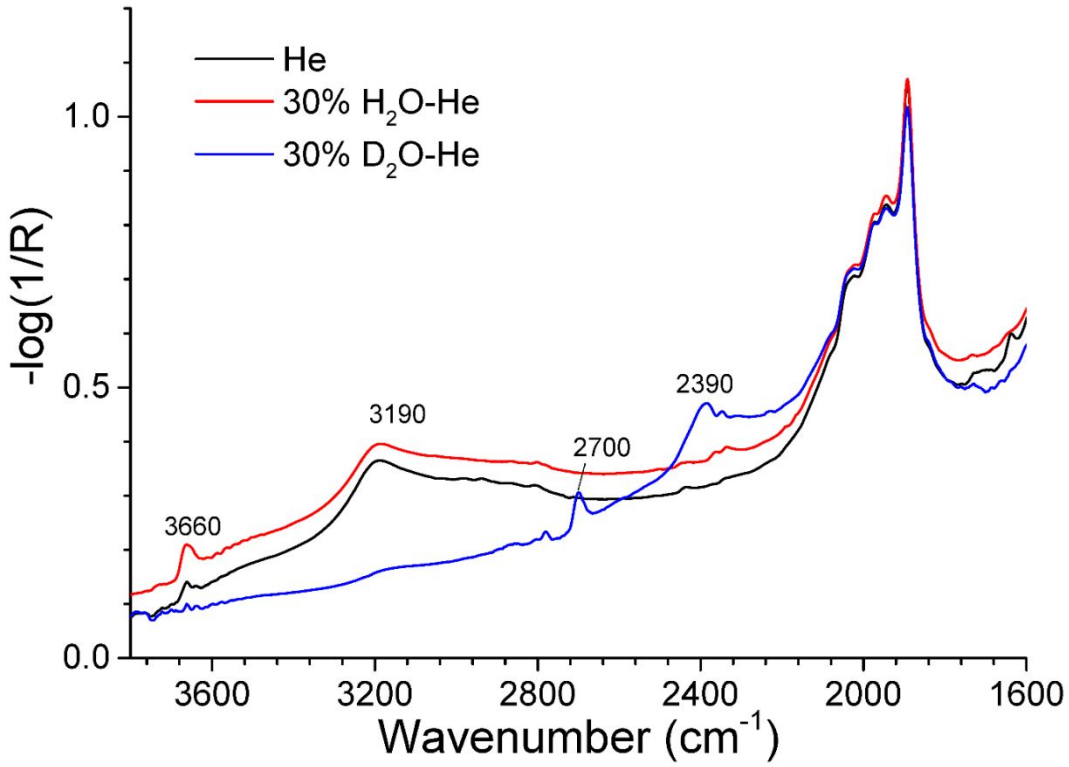

Figure 1. *In situ* DRIFT spectra of BaOP at 380 °C under He, 30%H_2O-He and 30%D_2O-He. The background corresponds to the spectrum of dehydrated KBr (the R reflectance is equal to I/I_{KBr}).

The DRIFT spectrum recorded under 30%H_2O-He flow at the same temperature was similar.

However, the absorbance of the ν(PO-H) band at 3660 cm^{-1} was increased evidencing formation of additional POH species. This phenomenon could arise from hydrolysis of the weak amount of α-$Ba_2P_2O_7$ leading to $BaHPO_4$. Note that the δ bending mode of chemisorbed H_2O at 1600-1630 cm^{-1} [39,40] was not observed showing such species was not present at the surface of BaOP sample. Isotopic labelling achieved under 30%D_2O-He at 380 °C led to a shift of the bands at 3660 and 3190 cm^{-1} to 2700 and 2390 cm^{-1}, respectively while the framework vibrational bands at 1850-2050 cm^{-1} remained unchanged. These shifts are close to the ones expected for deuteration of OH groups considering harmonic oscillator (ratios of 0.74 and 0.75, respectively instead of 0.73).

3.2 Modelling of the surfaces and influence of the water amount

The Brushite structure was built based on the neutron single crystal diffraction study[26] with a composition of 4 $CaHPO_4 \cdot 2H_2O$ and a C-centered monoclinic cell within the space group Cc (#9,C_s^4), as shown in Figure 2.

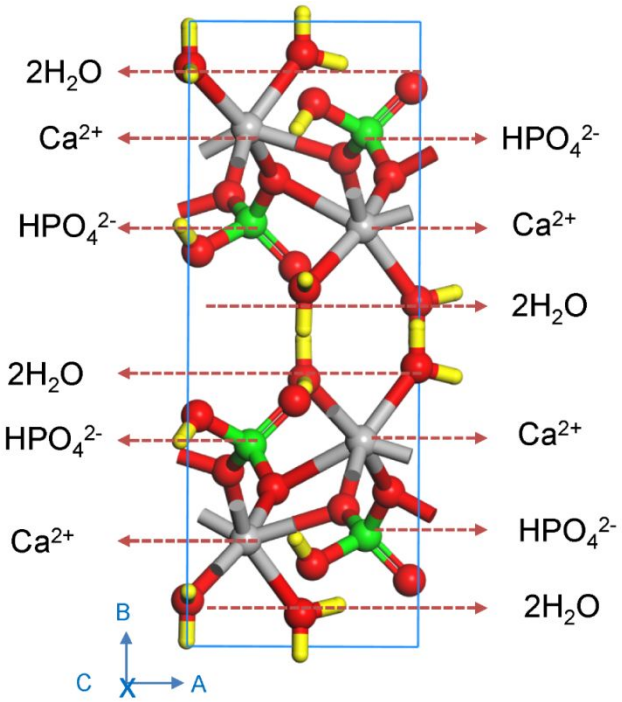

Figure 2. Unit cell of the layered structure of the Brushite, containing Ca atoms (grey), O atoms (red), H atoms (yellow) and P atoms (green).

The calculated cell parameters of a =5.98 Å, b = 15.14 Å and c = 6.24 Å, are in good agreement with the experimental ones (a_{exp} = 5.80 Å, b_{exp} = 15.13 Å, c_{exp} = 6.32 Å).[26] A detailed description of the brushite structure can be found in the Hirsch's work.[27]

The (010) surface of Brushite is the most stable surface computed (see computational details). As shown in Figure 3, the top of this surface is covered with eight water molecules per unit cell. We will consider later this as a complete monolayer of water, θ(H_2O)=1 ML. One can distinguish two orientations: (i) water marked W_a is perpendicular to the surface, 2.55 Å far away from the nearest Ca^{2+} atom, and gives a H bond to the O of HPO_4^{2-} and accepts an H bond from another water molecule nearby (ii) the other water, W_b, is parallel to the surface, closer to Ca^{2+} with a distance of 2.47 Å and is also involved in a H bond network, donating to HPO_4^{2-} and to W_a.

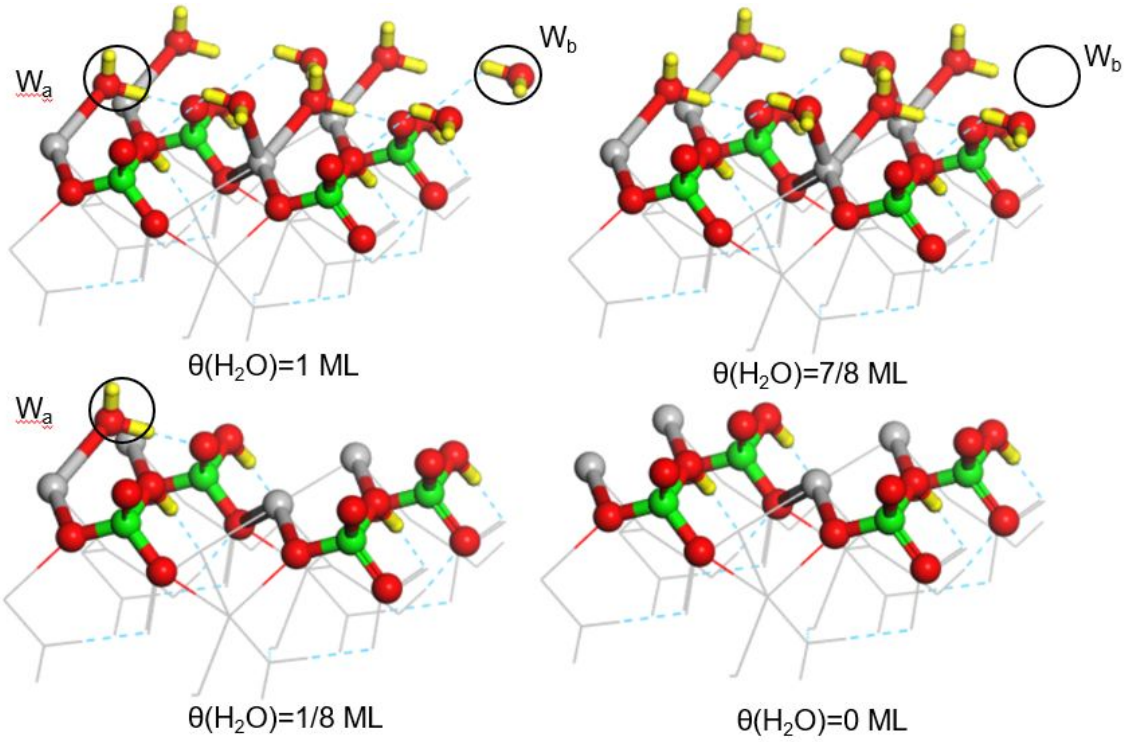

Figure 3. Structures of the (010) surface of $CaHPO_4 \cdot nH_2O$ with different water coverages, $\theta(H_2O)$=1 ML, 7/8 ML, 1/8 ML and 0 ML. Only half of the surface structure is shown here for simplicity. The two different types of water molecules are marked as W_a and W_b highlighted by a black circle in the top left structure, which corresponds to the structure obtained as cleaved from the bulk. The H bond network of W_a and W_b is shown in light blue dashed lines. At 1ML, 8 water molecules are found. At 7/8ML, one W_b water has been removed and the black circle indicates its former position. At 1/8ML, only one water molecule remains (W_a type) as highlighted by a black circle. Color-coding: grey for calcium, red for oxygen, green for phosphorus and yellow for hydrogen.

This highly hydrated surface can be easily dehydrated raising the temperature. The fully hydrated surface as cleaved from the bulk structure has a water coverage of $\theta(H_2O)$=1 ML, which corresponds to eight water molecules per unit cell. We considered various coverages in water, $\theta(H_2O)$=1 ML, 7/8 ML, 1/8 ML and 0 ML, as shown in Figure 3. To start, we generated a structure with a lower coverage of $\theta(H_2O)$=7/8 ML removing one water molecule. The structure with W_b deleted is -20 $kJ.mol^{-1}$ more stable than the one where W_a is deleted, thus only the surface with W_b deleted is shown in Figure 3. Next, we built a weakly hydrated surface, keeping only one water (W_a), reaching a coverage of $\theta(H_2O)$=1/8 ML. Finally, a fully dehydrated surface was also computed ($\theta(H_2O)$=0 ML), where the eight water molecules exposed at the external surface were deleted but the ones inside and in the bottom layers were still preserved. The relative stability of these surfaces as function of the temperature under 1 atm pressure of water is shown in Figure 4.

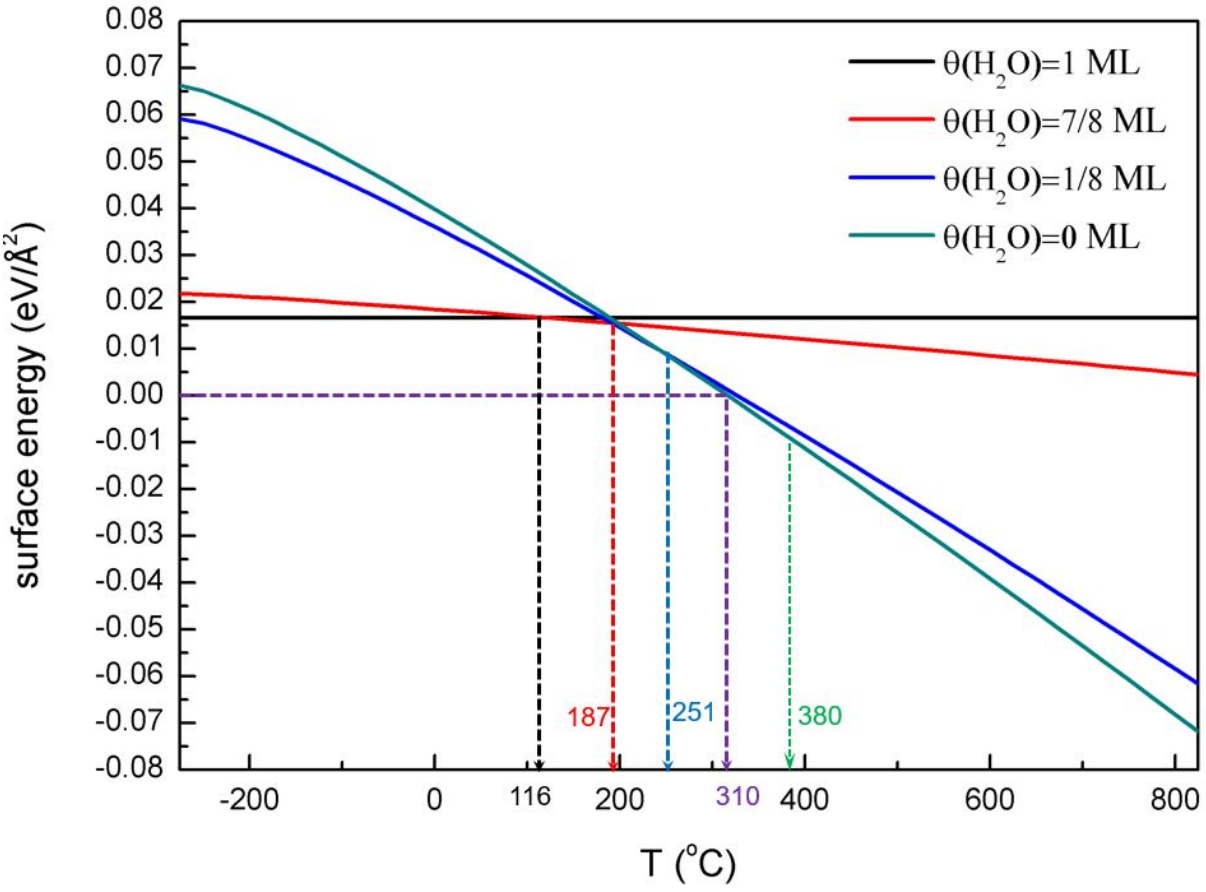

Figure 4. Surface energy in eV/Å^2 of Brushite (010) surfaces with various coverages (θ(H_2O)=1 ML, 7/8 ML, 1/8 ML and 0 ML) in water as function of the temperature and under a pressure in water of 1 atm.

When the temperature is lower than 116 °C, the surface prefers to be covered with water. At 116 °C, the surface starts to dehydrate, one W_b is desorbed and the exposed surface has a coverage of θ(H_2O)=7/8 ML. This temperature threshold for dehydration is consistent with the experimental one (80 °C) found by Dosen et al.[41] With an increase in the temperature, the dehydration keeps proceeding and at 187 °C, a coverage of θ(H_2O)=1/8 ML is reached and when the temperature is higher than 251 °C, the surface is totally dehydrated. It should also be noted that the surface energy becomes negative when the temperature is higher than 310 °C, which means that a dehydration of the bulk should occur. Such transformation to $CaHPO_4$ (Monetite)[14] was not further investigated

since the purpose was to build a model of the exposed facet of the BaOP catalyst. However, these temperatures of complete dehydration of the surface and of likely bulk dehydration are consistent with experimental observations where the transformation to Monetite is complete between 200 and 220 °C.[41] Based on the above discussion, it is clear that at the reaction temperature of 380 °C (which is also the IR spectrum recording temperature), the most favorable surface is the dehydrated surface. For experiments performed under 30%H_2O-He, we will include one water molecule to probe the impact of the modifications induced by the change of atmosphere and consider the $\theta(H_2O)$=1/8ML coverage.

As the amorphous layer lying over $Ba_3(PO_4)_2$ crystallites of the BaOP catalyst could be a phase with a general formula $Ba_{(1-x)}(HPO_4)_{1-2x}(H_2PO_4)_{2x}$ (see above), a defective surface was also constructed with a cationic vacancy and completed with two H^+. The most favorable structure of this defective surface is shown in Figure 5. The two additional H^+ are added on two HPO_4^{2-} yielding two $H_2PO_4^-$ groups. One of the additional H points down, forming an H bond with another HPO_4^{2-} deeper in the surface. This orientation is labeled H_{down}. The other additional H points up towards the gas phase and is labeled H_{up}. No other stable configuration can be found with the two additional H^+ pointing downward. The adsorption of water is not stronger on this Ca^{2+} vacancy than on the non- defective surface (adsorption energy of -84 kJ.mol^{-1} vs. -82 kJ.mol^{-1} respectively).

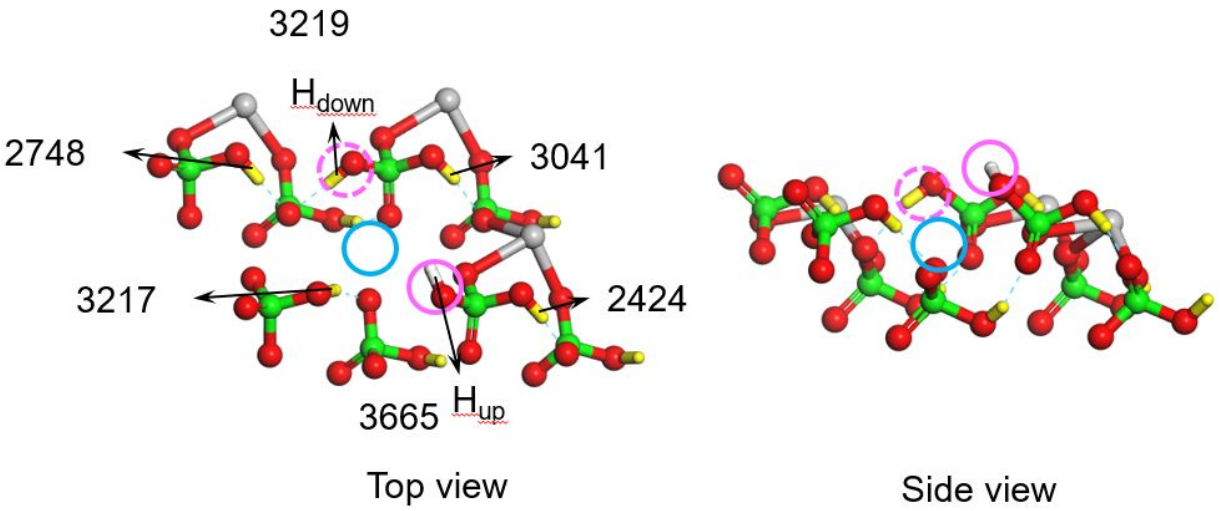

Figure 5. Computed structure of the defective surface. The Ca^{2+} vacancy is shown with a blue circle, the H_{down} with a pink dashed circle and H_{up} with a pink solid circle. The calculated wavenumbers (after rescaling as mentioned in the 2.3 section) of ν(PO-H) vibrations on the first layer are also shown nearby in cm^{-1}. Color-coding: grey for calcium, red for oxygen, green for phosphorus and yellow for hydrogen, except surface H_{up} which is marked in white.

To determine if the presence of the H_{up} pointing toward the gas phase appears as typical of the presence of a Ca^{2+} vacancy, we also investigated the likeliness of finding such an orientation in the non-defective fully dehydrated surface. The corresponding results are collected in Table 1. The most stable structure is Config 1, with four H_{down}, already discussed and shown in Figure 3. With one H_{up}, Config 2 is only 11 $kJ.mol^{-1}$ higher in energy, which corresponds to a Boltzmann probability of 0.15 at the working temperature of 380 °C. However, with four H_{up}, Config 3 is much less stable and is clearly very unlikely at this temperature. In other words, the presence of H_{up} cannot be attributed only to the presence of Ca^{2+} vacancy but is also related to thermal effects that favor the re-orientation of the PO-H bond.

Table 1. Influence of the PO-H orientation in the non-defective dehydrated (010) surface of Brushite on the stability at 380 °C and the computed wavenumbers of ν(PO-H), reported after rescaling as mentioned in the 2.3 section.

No.	Surface structure*	Relative energy /kJ.mol^{-1}	Boltzmann distribution	ν(PO-H_{up}) /cm^{-1}	ν(PO-H_{down}) /cm^{-1}
Config 1	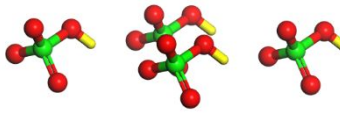	0	0.84	\	3170, 3161
Config 2	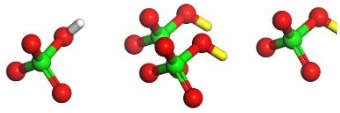	11	0.15	3691	3200-3133
Config 3	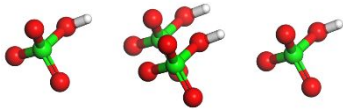	47	0.0002	3692	\

* H_{up} shown in white and H_{down} shown in yellow.

These two orientations (up and down) have a clear spectroscopic signature, with distinct ν(PO-H) stretching vibrations. In the non-defective dehydrated surface, the free PO-H_{up} is found to vibrate around 3690 cm^{-1} while the PO-H_{down} vibrations are red-shifted to the 3100-3200 cm^{-1} range due to their involvement in strong H-bonds with internal HPO_4^{2-} as shown in Table 1. In a defective surface, the vibration of free PO-H_{up} is around 3660 cm^{-1} and two vibrations of PO-H_{down} are around 3220 cm^{-1} (Figure 5). These two computed wavenumbers are in agreement with the observations reported in Figure 1 with two bands at 3660 and 3190 cm^{-1} identified as P-OH vibrations. However, in the defective surface, several ν(PO-H_{down}) wavenumbers are much lower (3041 cm^{-1}, 2748 cm^{-1} and 2424 cm^{-1}) due to the change of the environment induced by the deletion of one Ca^{2+} atom and the addition of two more protons on the HPO_4^{2-} groups leading to $H_2PO_4^-$. They could explain the large width of the band at 3190 cm^{-1} (see Figure 1) tailing to 2400 cm^{-1}.

This would imply that the surface of the BaOP catalyst was a defective hydrogen phosphate and hence contained $H_2PO_4^-$ species.

To further confirm the interpretation of the *in situ* DRIFT spectra of BaOP at 380 °C under He but also under 30%H_2O-He and 30%D_2O-He (Figure 1), we also considered the case with 1/8 ML of water (see Figure 4 and the corresponding discussion). The increase of the band at 3660 cm^{-1} in presence of water cannot be attributed to water itself since the δ bending mode of chemisorbed H_2O at 1600-1630 cm^{-1} [39,40] was not observed. However, all attempts to increase the amount of P-OH exposed thanks to water dissociation failed, on both the non-defective dehydrated and the defective surfaces. The only stable structure was obtained in the case of the non-defective surface (as shown in Figure S1) but it is 167 $kJ.mol^{-1}$ less stable than when water is not dissociated. Since the increase of the band at 3660 cm^{-1} cannot be attributed to water itself or to the increase of the number of POH by water dissociation, we checked if the stability of the P-OH_{up} could be increased by the presence of a chemisorbed water molecule: as shown in Table S2, turning one P-OH_{down} into a P-OH_{up} costs 9 $kJ.mol^{-1}$, which is very close to the 11 $kJ.mol^{-1}$ that was needed in absence of water (Table 1): the effect is not significant. Finally, we inferred that it could be related to hydrolysis of the small amount of α-$Ba_2P_2O_7$ present in the BaOP catalyst leading to $BaHPO_4$ formation and to an increase in the concentration of cationic vacancy in the hydrogen phosphate layer lying over $Ba_3(PO_4)_2$ crystallites, which would be favored by water. For $BaHPO_4$, the hydrolysis reaction is proposed to occur according to:

$$BaHPO_4 + H_2O \Rightarrow Ba_{(1-x)}(HPO_4)_{1-2x}(H_2PO_4)_{2x} + xBa^{2+} + 2xOH^-$$

Note that similar dissolution processes were reported in the liquid phase[42,43] and could be more favorable for sub-stoichiometric brushite containing cationic vacancies.

3.3 Acidity measurements by IR spectroscopy

The FTIR spectrum of pyridine adsorbed on BaOP plotted in Figure S2 (supplementary material) contained bands at 1614, 1592, 1574, 1489 and 1441 cm^{-1} which were attributed to pyridine coordinated to Lewis acid sites (LAS) or in H-bonding.[44,45] Observation of two 8a vibrational modes at 1614 and 1592 cm^{-1} revealed the presence of two different coordination sites. Considering their shifts compared to pyridine in liquid phase (1583 cm^{-1}), they were attributed to moderate Lewis acid and H-bonding sites, respectively. The three other bands corresponded to 8b, 19a and 19b modes, respectively.[44,45] The absence of band around 1540-1550 cm^{-1} typical of pyridinium cations indicated the absence of Brønsted acid sites able to protonate pyridine.

As pyridine (pKa=5.2) could be too weak to react with BAS, adsorption-desorption of lutidine (pKa=6.6) was followed by FTIR. Spectra recorded at different desorption temperatures are plotted in Figure 6.

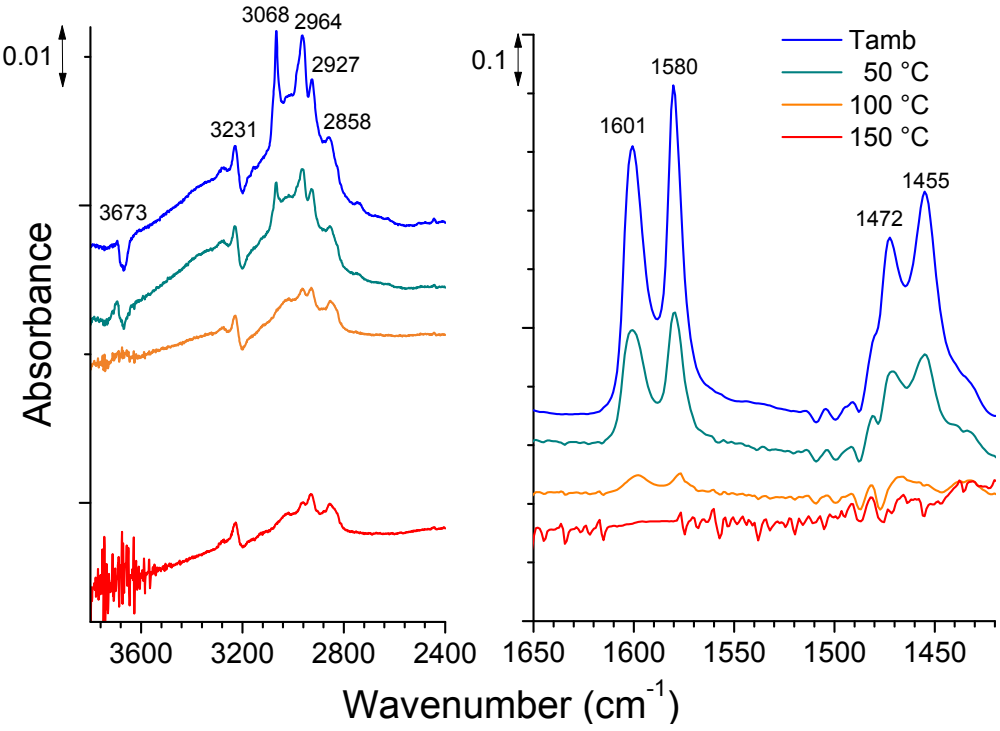

Figure 6. Evolution of the FTIR spectra of BaOP after adsorption of lutidine at T_{amb} and desorption under vacuum at increasing temperature.

At room temperature, bands were observed at 1601, 1580, 1472 and 1455 cm^{-1} which were attributed to the 8a, 8b, 19a and 19b vibrational modes of lutidine coordinated to LAS or in H-bonding[46,47] while the negative ν(PO-H) band at 3673 cm^{-1} revealed structural modifications of POH_{up} species that could arise from interaction between POH_{up} species and lutidine. It was not possible to know if the broad band around 3200 cm^{-1} and attributed to POH_{down} was affected because of superimposition of ν(CH_3) and ν(CH) stretching vibrations of lutidine. The 8a mode of lutidine is very sensitive to the adsorption mode and its small shift compared to the liquid phase (+7 cm^{-1}) was typical of H-bonded species. The 8a mode of lutidinium cations located at 1640-1655 cm^{-1} was not observed showing that POH species were not able to protonate lutidine. Increasing the desorption temperature, the bands of H-bonded lutidine disappeared in parallel to the negative ν(PO-H) band confirming their interdependence. The steric hindrance of methyl groups of lutidine could explain such molecule did not probe moderated LAS contrarily to pyridine.[47]

The *in situ* FTIR spectra recorded at adsorption equilibrium of NH_3 are shown on Figure 7 from 120 to 7 °C. They all contain one band at 1630 cm^{-1}, numerous bands between 3200 and 3400 cm^{-1} and a negative band at 3670 cm^{-1}. They disappeared above 200 °C in good agreement with TPD measurements. Comparison between the evolutions of the experimental coverage and the one calculated using the Temkin model (Figure S3) led to adsorption heat values of E_0= 65 $kJ.mol^{-1}$ and E_1 = 48 $kJ.mol^{-1}$. Such low values were typical of weak adsorption sites.[17]

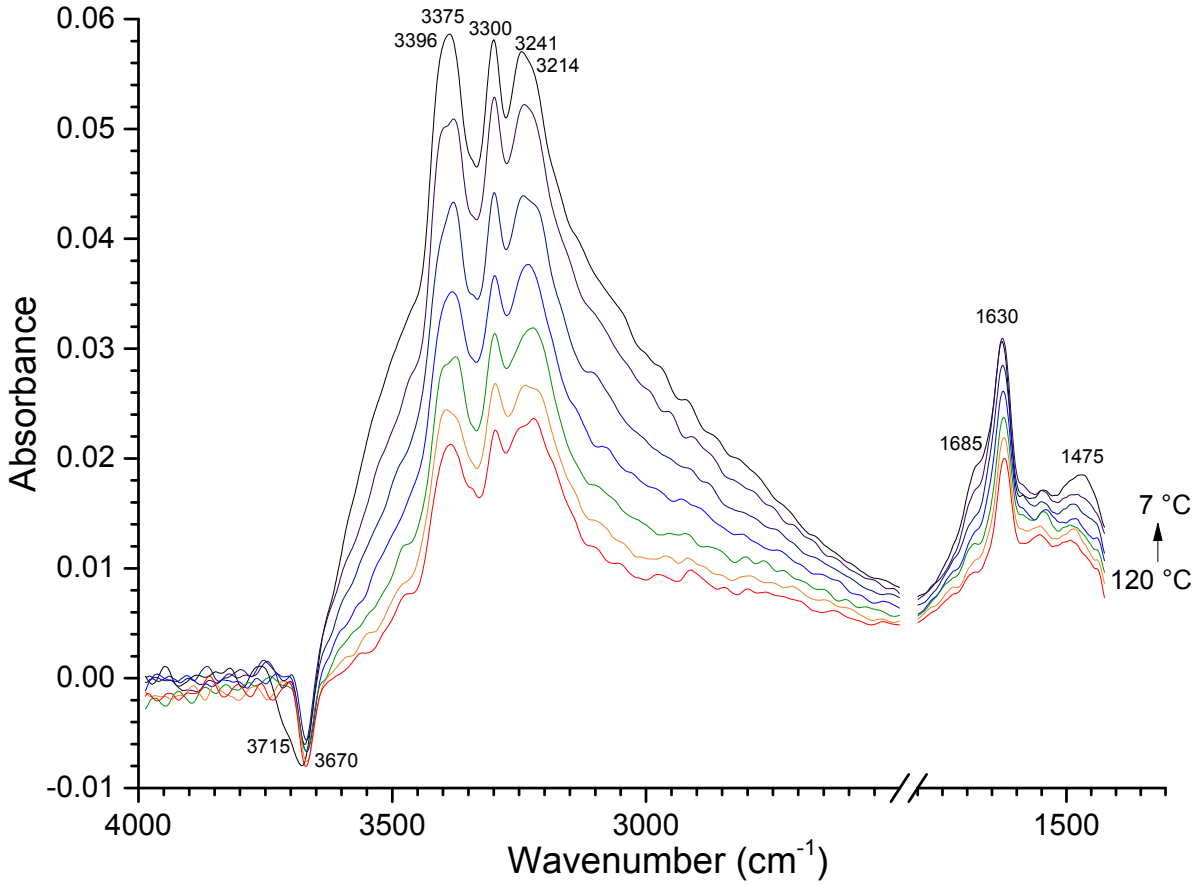

Figure 7. Evolution of the IR bands of NH_3 adsorbed species on pre-treated BaOP catalyst recorded under 2%NH_3-He flow from 120 to 7 °C. The backgrounds correspond to the spectra recorded after pretreatment under He flow at the same temperatures, mass of the pellet 53 mg.

We also established the relative stability of various ammonia surface concentrations as function of the temperature using ab initio thermochemistry (see Figure S4). When T < 145 °C, the coverage of NH_3 was $\theta(NH_3)$=1 ML (one ammonia per surface phosphate). It decreased to 1/2 ML from 145 °C to 162 °C. Above 162 °C, the surface was predicted to be bare, with no ammonia, in agreement with our experimental observations. To sustain the attribution of the bands and identify the corresponding sites, we show the most important predicted wavenumbers obtained on the dehydrated surfaces with a coverage of $\theta(NH_3)$=1/4 ML in Figure 8. The ones obtained with a

higher coverage, such as 1/2 ML, were found similar (see Table S3).

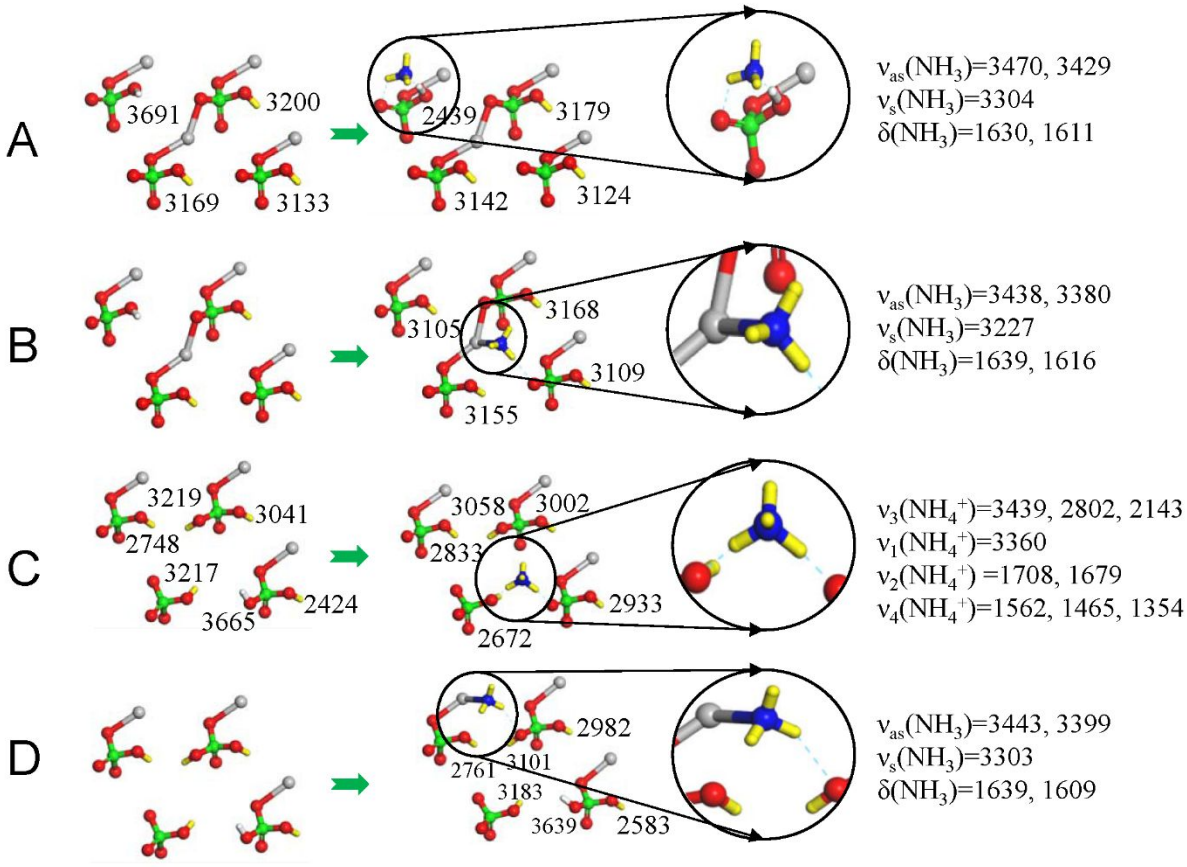

Figure 8. Structures (top view) and computed wavenumbers (in cm^{-1}) of the ν(PO-H) stretching vibrations and of the NH_3 or NH_4^+ vibrations after the adsorption of NH_3 on the non-defective dehydrated surface (A and B) and on the defective surface (C and D) at a coverage of $\theta(NH_3)$=1/4 ML. The corresponding adsorption energies are reported in Table 2. Color-coding: grey for calcium, red for oxygen, green for phosphorus, blue for nitrogen and yellow for hydrogen, except surface $H_{up,}$ which is marked in white.

The negative band at 3670 cm^{-1} indicated that POH_{up} species are modified by adsorbed NH_3. Thus, the adsorption of NH_3 was considered on the Config 2 of the non-defective surface (see Table 1), which presented some POH_{up} species, and on the defective surface. In both cases, the interaction with the BAS (the POH_{up}) and the LAS (Ca^{2+} in our model that stands for Ba^{2+} in the BaOP catalyst) were considered. The corresponding adsorption energies are provided in Table 2.

Table 2. Adsorption energy of water and ammonia on the non-defective and defective surface corresponding to the structures shown in Figure 8 and Figure 10. The adsorption of ammonia is given as a successive adsorption after the adsorption of water on structures E, F and G.

Label	Surface	Structure description	E_{ads} (H_2O) kJ.mol^{-1}	E_{ads} (NH_3) kJ.mol^{-1}
A	Non-defective	NH_3 is h-bounded to a P-OH_{up}	-	-48
B	Non-defective	NH_3 is in interaction with Ca^{2+}	-	-89
C	Defective	NH_4^+	-	-118
D	Defective	NH_3 is in interaction with Ca^{2+}	-	-84
E	Non defective	NH_3 is in interaction with Ca^{2+}	-90	-95
F	Non-defective	NH_4^+	-90	-46
G	Defective	NH_4^+	-82	-108

With a low adsorption energy (-48 kJ.mol^{-1}), the adsorption on the BAS (structure A) is less likely than on the LAS of the dehydrated non-defective surface (structure B, -89 kJ.mol^{-1}). The contrast between these two site types is likely to be reduced since here we modeled Ba^{2+} by a stronger LAS, namely Ca^{2+}. On the defective surface, it was the opposite situation with an adsorption on the LAS (structure D, -84 kJ.mol^{-1}) less stabilizing than on the BAS (structure C, -118 kJ.mol^{-1}), a difference that is expected to be even stronger for the weak LAS Ba^{2+}. In this defective case, the adsorbed NH_3 even captured

a proton of $H_2PO_4^-$ yielding NH_4^+, H bonded with several nearby oxygen atoms. Conversely, the generation of NH_4^+ from the proton transfer from HPO_4^{2-} to NH_3 was found to be very unlikely on the non-defective dehydrated surface with an adsorption energy much weaker than the non-dissociative adsorption (-12 kJ.mol^{-1} vs. -89 kJ.mol^{-1}, Figure S5).

The experimental spectra contained one band at 1630 cm^{-1} typical of Lewis coordination and/or H-bonding ($\delta(NH_3)$ vibration).[48] This vibration mode is doubly degenerated in free NH_3 but non-symmetric environment slightly split the band in the computed spectra. It was predicted to be not sensitive to the type of interaction since it was computed at 1630, 1611 cm^{-1} when NH_3 was H-bonded to P-OH_{up} (Figure 8A) and at 1639, 1609 cm^{-1} when NH_3 was in interaction with a LAS (Figure 8B and D). The $\nu(NH_3)$ stretching vibrations were more sensitive to the adsorption site. The symmetric mode was strongly red-shifted (3227 cm^{-1}) when NH_3 was in interaction with the LAS on the non-defective surface (Figure 8B) compared with cases where it was in interaction with the same site on the defective surface (3303 cm^{-1}, Figure 8D) or H-bonded to PO-H_{up} of the non-defective surface (3304 cm^{-1}, Figure 8A). The asymmetric vibrations were all found in a range of 3380-3470 cm^{-1}. All these bands were compatible with the experimental observation of a rather complicated 3200-3400 cm^{-1} spectral range with bands at 3396, 3375, 3300, 3241 and 3214 cm^{-1} superimposed to an asymmetric broad one (Figure 7). The first two were attributed to $\nu_{asym}(NH_3)$ vibrations and the third one to $\nu_{sym}(NH_3)$. Note that $\nu_{asym}(NH_3)$ vibrations are doubly degenerated for free NH_3 (E mode). Observation of two $\nu_{asym}(NH_3)$ bands and one $\nu_{sym}(NH_3)$ band implies a symmetry lowering compared to C_{3v}. Attribution of the two last bands at 3241 and 3214 cm^{-1} was

not obvious since it could either correspond to overtones of $\delta_{asym}(NH_3)$ and to $\nu_1(NH_4^+)$ vibrations[49,50] but also to $\nu_{sym}(NH_3)$ with NH_3 in interaction with the Lewis site on the non-defective surface (3227 cm^{-1}, Figure 8B) or to ν(PO-H) vibrations of POH_{down} species. As these bands were kept upon heating to 120 °C while $\nu_4(NH_4^+)$ at 1475 cm^{-1} [49,50] disappeared above 7 °C, attribution to $\nu_1(NH_4^+)$ was ruled out.

Observation of broad band tailing to 2400 cm^{-1} strongly suggested higher contribution of ν(PO-H) vibrations due to POH_{down}. Indeed, some POH_{down} vibrations were predicted to be red-shifted by the NH_3 absorption with bands shifting from 3169 to 3139 cm^{-1} for instance (see Figure 8A). In addition, the presence of Ca^{2+} vacancies in the defective structure would also yield to the observation of vibrations as low as 2583 cm^{-1} related to the presence of $H_2PO_4^-$ species (Figure 8D). Last, when NH_3 was H bonded directly to $PO\text{-}H_{up}$ (Figure 8A), the $\nu(PO\text{-}H_{up})$ band at 3691 cm^{-1} shifted down to 2439 cm^{-1} due to the strong H-bond. This corresponds to a zone where a small absorbance was seen in the experimental spectra. The orientation of the $PO\text{-}H_{up}$ was also affected in the case of an interaction of NH_3 with the LAS, despite the lack of direct interaction. It rotated from up to down, inducing a strong red shift of $\nu(PO\text{-}H_{up})$ from 3691 to 3105 cm^{-1} and the red shift of the three $\nu(PO\text{-}H_{down})$ to 3100-3200 cm^{-1} as shown in Figure 8B and D. This is in line with the experimental observations regarding the disappearing of the band at 3670 cm^{-1} and the broad band in the range of 2800-3200 cm^{-1}. Finally, the band at 3241 cm^{-1} could correspond to the $\nu_{sym}(NH_3)$ vibration of NH_3 adsorbed on the LAS of the non-defective surface while the shoulder at 3214 cm^{-1} would be assigned to changes in the POH_{down} signature. Attribution of the bands 3241 and 3214 cm^{-1} to two different species (adsorbed NH_3 and POH_{down}, respectively) was confirmed by the change of their relative intensity with the temperature (Figure 7).

The negative shoulder observed at 3715 cm^{-1} only on the spectrum recorded to 7 °C (below

RT) was assigned to $\nu(H_2O)$ due to traces of physisorbed water leading to the spontaneous reaction:[16,39]

$$NH_3 + H_2O_{ads} \Leftrightarrow (NH_4^+)_{ads} + OH^-_{ads}$$

Such reaction which did occur only at 7 °C also explained observation of the bending $\nu_4(NH_4^+)$ and $\nu_2(NH_4^+)$ vibrations bands at 1475 and 1685 cm^{-1}, respectively.[49,50] The latter one is observed by IR only when symmetry of NH_4^+ cations is lower than T_d.[49,50] DFT computations provided another possible explanation on NH_4^+ formation. Indeed, traces of physisorbed water at low temperature could increase the amount of Ca^{2+} vacancies (see section 3.2), which promotes the formation of NH_4^+. Their presence was predicted on the defective surface, with strong adsorption energy of -118 $kJ.mol^{-1}$ (Table 2). The computed NH_4^+ vibration bands were split by the environment. By comparison with the observed ones (1475 and 1685 cm^{-1}), two bands were found to be the major ones (1465 and 1679 cm^{-1}, see Figure 8C).

To sum up, the interaction of NH_3 with the POH groups by H-bonding without significant protonation of the non-defective surface could not be discarded based on the infrared signature. However, it was found to be less likely based on energetic consideration since it had the weakest adsorption energy (Table 2). Even upon interaction with the LAS, the $\nu(PO\text{-}H_{up})$ band was found to disappear due to the re-orientation of the PO-H bond downward. Bands at 3396-3375, 3300, 3241 and 3214 cm^{-1} were attributed to degenerated $\nu_{asym}(NH_3)$, $\nu_{sym}(NH_3)$ of NH_3 in interaction with the LAS of the defective surface, $\nu_{sym}(NH_3)$ of NH_3 in interaction with the LAS of the non-defective surface and to $\nu(PO\text{-}H_{down})$ respectively. The broad band tailing at 2400 cm^{-1} was due to the reorganization of the $PO\text{-}H_{down}$ upon adsorption.

3.4 Water effect on acidity

In situ acidity measurements were achieved at adsorption equilibrium under 1%NH_3-3%H_2O-He flow and FTIR spectra are plotted in Figure 9. The absorbance value of the $\nu_4(NH_4^+)$ band at 1458 cm^{-1} was strongly increased evidencing a higher Brønsted acidity formed under water vapor.[20,39] As the band at 1640 cm^{-1} could be attributed to either $\delta(NH_3)$ and $\delta(H_2O)$ vibrations and as no $\nu_{asym}(NH_3)$ vibrations around 3300-3400 cm^{-1} were distinguishable from the broad band at 3420 cm^{-1} due to $\nu(H_2O)$ of chemisorbed water, the presence of chemisorbed NH_3 species remained questionable. Note that the shoulder observable at 3220 cm^{-1} above 40 °C could be attributed to $\nu_1(NH_4^+)$ vibrations associated with $\nu_4(NH_4^+)$ at 1458 cm^{-1}.[49,50] Finally, the small band at 3692 cm^{-1} can correspond to $\nu(PO\text{-}H_{up})$ and to $\nu(H_2O_{ads})$ as already discussed earlier.

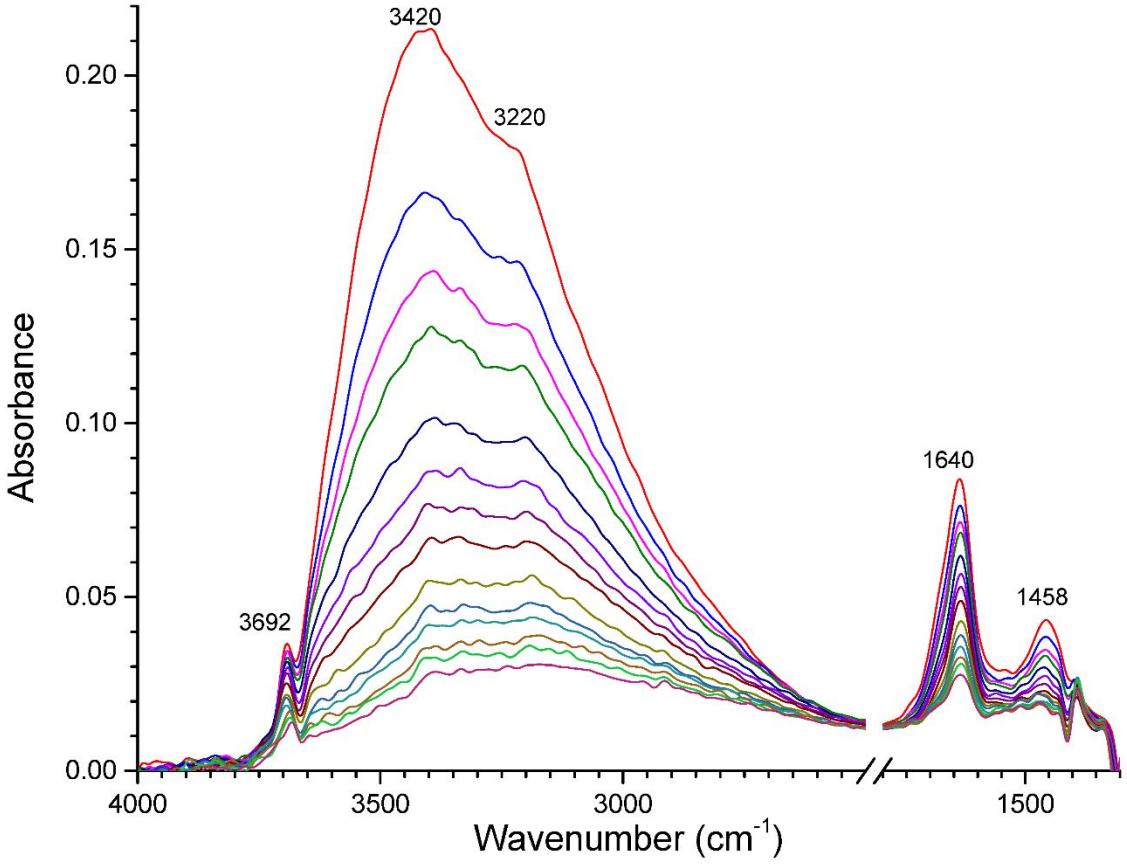

Figure 9. Evolution of the IR bands of NH_3 adsorbed species on pre-treated BaOP catalyst recorded under 1%NH_3-3%H_2O-He flow from 172 to 28 °C. The backgrounds correspond to the spectra recorded after pretreatment under He flow at the same temperatures, mass of the pellet 53 mg.

DFT computations provided an atomistic view of the adsorption of ammonia on the BAS and the LAS of both the non-defective and defective surface, but including water co-adsorption ($\theta(H_2O)$=1/8 ML) assuming that the presence of ammonia does not modify strongly the predicted water coverage. The corresponding structures along with their wavenumbers are shown in Figure 10 and the adsorption energies are reported in Table 2. The computed vibrations of the three structures are compatible with the experimental observations.

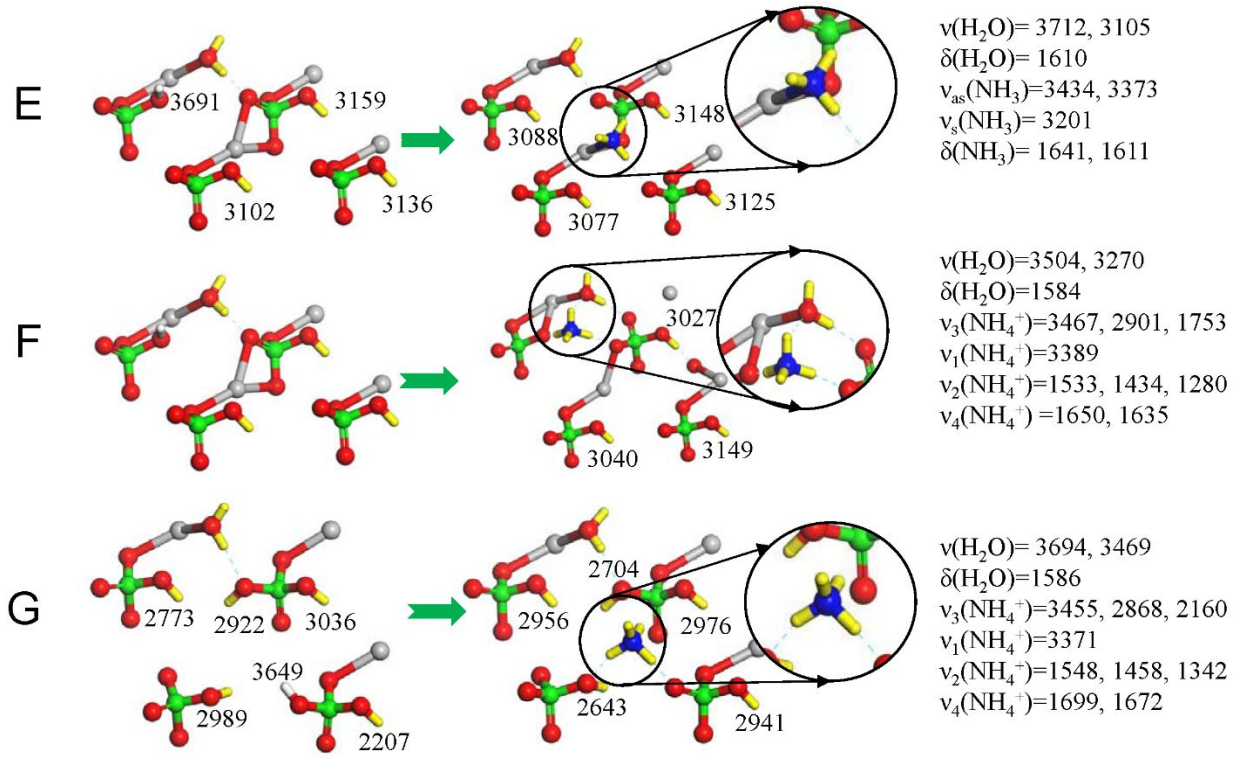

Figure 10. Structures and computed wavenumbers (in cm^{-1}) of the ν(PO-H) stretching vibrations, water vibration and of the NH_3 or NH_4^+ vibration after the adsorption of NH_3 on the non-defective dehydrated surface (E and F) and on the defective surface (G). The corresponding adsorption energies are reported in Table 2. Color-coding: grey for

calcium, red for oxygen, green for phosphorus, blue for nitrogen and yellow for hydrogen, except surface H_{up} which is marked in white.

On the non-defective surface, the presence of a water molecule does not modify the interaction of NH_3 with the LAS site (structure E), which was still found being the most stable adsorption site with adsorption energy of -95 kJ.mol^{-1} (Table 2). Noticeably, the P-OH_{up} shifts to a P-OH_{down} during this adsorption despite the absence of a direct interaction with NH_3, yielding to a predicted disappearance of the vibration at 3691cm^{-1} but with the appearance of a band at 3712 cm^{-1} related to the elongation of OH in the chemisorbed water. In other words, while the presence of NH_3 was questionable based on the experimental spectrum, it seems rather likely at distance of defective sites since structure E is more stable than the ones yielding to ammonium following a proton transfer from water or the BAS of the surface. Still, co-adsorbed water made the BAS more acidic. Indeed, interaction of NH_3 with the PO-H_{up} generated NH_4^+ (structure F) with adsorption energy of -46 kJ.mol^{-1} (Table 2), a process strongly facilitated by the presence of water even if it does not participate directly, thanks to an extra stabilizing H bond. On the totally dehydrated surface, the same reactive adsorption yielded only to adsorption energy of -22 kJ.mol^{-1}. This could explain the increase of the NH_4^+ band absorption in presence of ammonia co-fed with water in comparison with ammonia only. Another source of NH_4^+ could be the increase of Ca^{2+} vacancies promoted by the presence of water (see section 3.2) since NH_3 easily turns into NH_4^+ by capturing the proton of the $H_2PO_4^-$ group close to the Ca^{2+} vacancy (structure G), with strong adsorption energy of -108 kJ.mol^{-1} (Table 2).

4. CONCLUSIONS

In this work, acidic properties of BaOP catalyst were investigated combining FTIR spectra achieved at the dehydrated state and under water vapour and DFT calculations. Such catalyst efficient for the dehydration of lactic acid to acrylic acid was previously shown to contain a surface mono/dihydrogen phosphate amorphous layer composed by Ba^{2+} cations, P=O and POH groups. Therefore, the surface layer was simulated by non-defective and defective MPOH structure. Adsorption of pyridine, lutidine and NH_3 at the surface of BaOP catalyst revealed the presence of moderate LAS and of POH groups without significant protonation for the first two probe molecules. Ammonia was found to mainly interact with the LAS on both the non-defective surface and the defective surface while the PO-H_{up} surface groups are reoriented downward. Formation of BAS was shown to occur under water vapor by co-adsorption of NH_3 and H_2O. The phenomenon cannot be explained by dissociation of H_2O molecules as shown by DFT calculations. In fact, the presence of water does not modify the interaction of NH_3 with the LAS sites of non-defective surface but made the BAS more acidic. The presence of water could also promote formation of defective surface and hence $H_2PO_4^-$ groups which easily react with NH_3 to form NH_4^+.

ASSOCIATED CONTENT

The Supporting Information is available free of charge on the ACS Publications website at DOI: XXX

Scaling factor of NH_3 vibrational modes, Influence of the PO-H orientation in the non-defective partially hydrated (010) surface ($\theta(H_2O)$=1/8 ML) on the stability at 380 °C and the computed wavenumbers of ν(PO-H), wavenumbers of NH_3 and NH_4^+ co-adsorption on defective surface, dissociated H_2O on defective surface, Structure of the dissociated H_2O on the non-defective surface, FTIR spectrum of adsorbed pyridine, Experimental evolutions of the coverage of the NH_3 adsorbed species with the adsorption temperature and theoretical curve obtained using Temkin

model; surface energy in eV/Å^2 of Brushite (010) surfaces with various coverages; possible configuration of the ammonium cation on a dehydrated surface; archive of raw data from computations including structures and frequencies.

AUTHOR INFORMATION

Corresponding Authors

*E-mail: stephane.loridant@ircelyon.univ-lyon1.fr

*E-mail: carine.michel@ens-lyon.fr

ORCID

Stéphane Loridant: 0000-0001-8590-433X

Carine Michel: 0000-0002-4501-7194

Notes

The authors declare no competing financial interest.

ACKNOWLEDGEMENTS

This work was supported by French ANR Program Chimie Durable–Industries–Innovation (CD2I) GALAC, a joint project between IRCELYON, UCCS, LC/ENS-Lyon and Novance company. Laurent Piccolo is acknowledged for access to the IR apparatus founded by the project DINAMIC (reference ANR-2011-BS10-009).

REFERENCES

(1) Mäki-Arvela, P.; Simakova, I.L.; Salmi, T.; Murzin, D.Y. Production of lactic acid/lactates from biomass and their catalytic transformations to commodities. *Chem. Rev.* **2013**, *114*, 1909–1971.

(2) Blanco, E.; Loridant, S.; Pinel, C. Valorization of lactic acid and derivatives to acrylic acid derivatives: review of mechanistic studies. In *Reaction Pathways and Mechanisms in Thermocatalytic Biomass Conversion II*, Schlaf, M.; Zhang, Z. C., Eds.; Springer, 2016, Chapter 3, pp39–62.

(3) Sun, D.; Yamada, Y.; Sato, S.; Ueda, W. Glycerol as a potential renewable raw material for acrylic acid production. *Green Chem.* **2017**, *19*, 3186–3213.

(4) Chieregato, A.; Soriano, M.D.; Basile, F.; Liosi, G.; Zamora, S.; Concepcion, P.; Cavani, F. Lopez Nieto, J.M. One-pot glycerol oxydehydration to acrylic acid on multifunctional catalysts: Focus on the influence of the reaction parameters in respect to the catalytic performance. *Appl. Catal. B: Environ.* **2014**, *150-151*, 37–46.

(5) Chieregato, A.; Soriano, M.D.; Garcia-Gonzalez, E.; Puglia, G.; Basile, F.; Concepcion, P.; Bandinelli, C.; Lopez Nieto, J.M.; Cavani, F. Multielement Crystalline and Pseudocrystalline Oxides as Efficient Catalysts for the Direct Transformation of Glycerol into Acrylic Acid. *ChemSusChem* **2015**, *8*, 398-406.

(6) Fan, Y.; Zhou, C.; Zhu, X. Selective Catalysis of Lactic Acid to Produce Commodity Chemicals, *Catal. Rev.* **2009**, *51*, 293–324.

(7) Abdel-Rahman, M.A.; Tashiro, Y.; Sonomoto, K. Lactic acid production from lignocellulose-derived sugars using lactic acid bacteria: Overview and limits. *BioTech. Adv.* **2013**, *1*, 877–902.

(8) Abdel-Rahman, M.A.; Tashiro, Y.; Sonomoto, K. Recent advances in lactic acid production by microbial fermentation processes. *J. Biotech.* **2011**, *156*, 286–301.

(9) Auneau, F.; SadrArani, L.; Besson, M.; Djakovitch, L.; Michel, C.; Delbecq, F.; Sautet, P.; Pinel, C.; Heterogeneous Transformation of Glycerol to Lactic Acid. *Top.Catal.* **2012**, *55*, 474.

(10) https://www.businesswire.com/news/home/20170621005594/en/Global-Lactic-Acid-Market-2017-2025---Growth

(11) Blanco, E.; Delichere, P.; Millet, J.M.M.; Loridant, S. Gas phase dehydration of lactic acid to acrylic acid over alkaline-earth phosphates catalysts. *Catal. Today*, **2014**, *226*, 185–191.

(12) Blanco, E.; Lorentz, C.; Delichere, P.; Burel, L.; Vrinat, M.; Millet, J.M.M.; Loridant, S. Dehydration of ethyl lactate over alkaline earth phosphates: Performances, effect of water on reaction pathways and active sites, *Appl. Catal. B: Environ.* **2016**, *180*, 596–606.

(13) Hammaecher, C.; Paul, J.-F. Density functional theory study of lactic acid adsorption and dehydration reaction on monoclinic 011, $\bar{1}01$, and $\bar{1}11$ zirconia surfaces. *J. Catal.* **2013**, *300*, 174–182.

(14) Dorozhkin S.V.; Epple, M. Biological and Medical Significance of Calcium Phosphates, *Angew. Chem. Int. Ed.* **2002**, *41*, 3130 – 3146.

(15) Chafik, T.; Dulaurent, O.; Gass, J.L.; Bianchi, D. Heat of Adsorption of Carbon Monoxide on a $Pt/Rh/CeO_2/Al_2O_3$ Three-Way Catalyst Using in-Situ Infrared Spectroscopy at High Temperatures. *J. Catal.* **1998**, *179*, 503–514.

(16) Giraud, F.; Couble, J.; Geantet, C.; Guilhaume, N.; Puzenat, E.; Gros, S.; Porcheron, L.; Kanniche, M.; Bianchi, D. Experimental Microkinetic Approach of De-NOx by NH_3 on $V_2O_5/WO_3/TiO_2$ Catalysts. 4. Individual Heats of Adsorption of Adsorbed H_2O Species on Sulfate-Free and Sulfated TiO_2 Supports. *J. Phys. Chem.C* **2015**, *119*, 16089–16105.

(17) Giraud, F.; Geantet, C.; Guilhaume, N.; Gros, S.; Porcheron, L.; Kanniche, M.; Bianchi, D. Experimental Microkinetic Approach of De-NOx by NH_3 on $V_2O_5/WO_3/TiO_2$ Catalysts. 1.

Individual Heats of Adsorption of Adsorbed NH_3 Species on a Sulfate-Free TiO_2 Support Using Adsorption Isobars. J. Phys. Chem. C **2014**, *118*, 15664–15676.

(18) Giraud, F.; Geantet, C.; Guilhaume, N.; Loridant, S.; Gros, S.; Porcheron, L.; Kanniche, M.; Bianchi, D. Experimental Microkinetic Approach of De-NOx by NH_3 on $V_2O_5/WO_3/TiO_2$ Catalysts. 2. Impact of Superficial Sulfate and/or V_xO_y groups on the Heats of Adsorption of Adsorbed NH_3 Species. J. Phys. Chem. C **2014**, *118*, 15677−15692.

(19) Giraud, F.; Geantet, C.; Guilhaume, N.; Loridant, S.; Gros, S.; Porcheron, L.; Kanniche, M.; Bianchi, D. Experimental Microkinetic Approach of De-NOx by NH_3 on $V_2O_5/WO_3/TiO_2$ Catalysts. 3. Impact of Superficial WO_z and V_xO_y/WO_z Groups on the Heats of Adsorption of Adsorbed NH_3 Species. J. Phys. Chem. C **2015**, *119*, 15401−15413.

(20) Buniazet, Z.; Couble, J.; Bianchi, D.; Rivallan, M.; Cabiac, A.; Maury, S.; Loridant, S. Unravelling water effects on solid acid catalysts: Case study of TiO_2/SiO_2 as a catalyst for the dehydration of isobutanol, J. Catal. **2017**, *348*, 125–134.

(21) Kresse, G.; Furthmüller, J. Efficient iterative schemes for ab initio total-energy calculations using a plane-wave basis set. *Phys. Rev. B-Condens. Matter Mater. Phys.* **1996**, *54*, 11169–11186.

(22) Kresse, G.; Furthmüller, J. Efficiency of ab-initio total energy calculations for metals and semiconductors using a plane-wave basis set. *Comput. Mater. Sci.* **1996**, *6*, 15–50.

(23) Kresse, G.; Hafner, J. *Ab initio* molecular dynamics for liquid metals. *Phys. Rev. B - Condens. Matter Mater. Phys.* **1993**, *47*, 558–561.

(24) Perdew, J. P.; Burke, K.; Ernzerhof, M. Generalized Gradient Approximation Made Simple. *Phys. Rev. Lett.* **1996**, *77,* 3865–3868.

(25) Kresse, G.; Joubert, D. From ultrasoft pseudopotentials to the projector augmented-wave method. *Phys. Rev. B-Condens. Matter Mater. Phys.* **1999**, *59*, 1758–1775.

(26) Curry, N.A.; Jones, D. W. Crystal Structure of Brushite, Calcium Hydrogen Orthophosphate Dihydrate: A Neutron-diffraction Investigation. *J. Chem. Soc. A* **1971**, 3725−3729.

(27) Hirsch, A., Azuri, I., Addadi, L., Weiner, S., Yang, K., Curtarolo, S., Kronik, L. Infrared Absorption Spectrum of Brushite from First Principles. *Chem. Mater*. **2014**, 26, 2934-2942.

(28) Schofield, P.F.; Knight, K.S.; van der Houwen, J.A.M.; Valsami-Jones, E. The role of hydrogen bonding in the thermal expansion and dehydration of brushite, di-calcium phosphate dihydrate *Phys. Chem. Minerals* **2004**, 31, 606–624.

(29) Kumta, P.N.; Sfeir, C.; Lee, D.-H.; Olton, D.; Choi, D. Nanostructured calcium phosphates for biomedical applications: novel synthesis and characterization, *Acta Biomaterialia*, **2005**, *1*, 65–83.

(30) Baroni, S.; Giannozzi, P.; Testa, A. Green's-Function Approach to Linear Response in Solids. *Phys. Rev. Lett.* **1987**, *58*, 1861–1894.

(31) Bauer, T.; Maisel, S.; Blaumeiser, D.; Vecchietti, J.; Taccardi, N.; Wasserscheid, P.; Bonivardi, A.; Görling, A.; Libuda, J. *ACS Catal.* **2019**, *9*, 2842−2853.

(32) Anggara, T.; Paolucci, C.; Schneider, W.F. *J. Phys. Chem. C* **2016**, *120*, 27934−27943.

(33) Chizallet, C.; Costentin, G. ; Che, M. ; Delbecq, F. ; Sautet, P. *J. Am. Chem. Soc.* **2007**, *129*, 6442-6452.

(34) Cheng, Z.H.; Yasukawa, A.; Kandori, K.; Ishikawa, T. FTIR Study on incorporation of CO_2 into calcium hydroxyapatite. *J. Chem. Soc., Faraday Trans.* **1998**, *94*, 1501–1505.

(35) Trchova, M.; Capkova, P.; Matejka, P.; Melanova, K.; Benes, L. Study of Host–Guest Interactions in Intercalate $Zr(HPO_4)_2{\cdot}2CH_3CH_2OH$ using a Combination of Vibration Spectroscopy and Molecular Simulations. *J. Solid State Chem.* **1999**, *145*, 1–9.

(36) Koleva, V.; Stefov, V.; Cahil, A.; Najdoski, M.; Soptrajanov, B.; Engelen, B.; Lutz, H.D.

Infrared and Raman studies of manganese dihydrogen phosphate dihydrate, $Mn(H_2PO_4)_2.2H_2O$. Part II: Region of the internal OH group vibrations. *J. Mol. Struct.* **2009**, *919*, 164–169.

(37) Frost, R.L.; Xi, Y.; Palmer, S.J.; Tan, K. Millar, G.J. Vibrational spectroscopy of synthetic archerite $(K,NH_4)H_2PO_4^-$ and in comparison with the natural cave mineral. *J. Mol. Struct.* **2012**, *1011*, 128–133.

(38) Frost, R.L.; Palmer, S.J.; Xi, Y. A Raman spectroscopic study of the mono-hydrogen phosphate mineral dorfmanite $Na_2(PO_3OH)\cdot 2H_2O$ and in comparison with brushite. *Spectrochim. Acta Part A* **2011**, *82*, 132–136.

(39) Giraud, F.; Couble, J.; Geantet, C.; Guilhaume, N.; Puzenat, E.; Gros, S.; Porcheron, L.; Kanniche, M.; Bianchi, D. Experimental Microkinetic Approach of De-NOx by NH_3 on $V_2O_5/WO_3/TiO_2$ Catalysts. 4. Individual Heats of Adsorption of Adsorbed H_2O Species on Sulfate-Free and Sulfated TiO_2 Supports. J. Phys. Chem. C **2015**, *119*, 16089−16105.

(40) Buniazet, Z.; A. Cabiac, S. Maury, D. Bianchi, S. Loridant, Unexpected selectivity of ferrierite for the conversion of isobutanol to linear butenes and water effects, *Appl. Catal. B: Environmental* **2019**, *243*, 594–603.

(41) Dosen, A.; Giese, R.F. Thermal decomposition of brushite, $CaHPO_4\cdot 2H_2O$ to monetite $CaHPO_4$ and the formation of an amorphous phase, *American Mineralogist*, **2011**, *96*, 368–373.

(42) Lagno, F.;. Rocha, S.D.F; Katsarou, L.; Demopoulos, G.P. Supersaturation-Controlled Synthesis of Dicalcium Phosphate Dihydrate and Nanocrystalline Calcium-Deficient Hydroxyapatite, *Ind. Eng. Chem. Res.* **2012**, *51*, 6605−6612.

(43) Wang, L.; Nancollas, G.H. Calcium Orthophosphates: Crystallization and Dissolution, *Chem. Rev.* **2008**, *108*, 4628–4669.

(44) Busca, G. The surface acidity of solid oxides and its characterization by IR spectroscopic

methods. An attempt at systematization *Phys. Chem. Chem. Phys.* **1999**, *1*, 723–736.

(45) Busca, G. Spectroscopic characterization of the acid properties of metal oxide catalysts. *Catal. Today* **1998**, *41*, 191–206.

(46) Oliviero, L.; Vimont, A.; Lavalley, J.-C.; Romero Sarria, F.; Gaillard, M.; Mauge, F. 2,6-Dimethylpyridine as a probe of the strength of Brønsted acid sites: study on zeolites. Application to alumina. *Phys. Chem.Chem. Phys.* **2005**, *7*, 1861–1869.

(47) Onfroy, T.; Clet, G.; Houalla, M. Quantitative IR characterization of the acidity of various oxide catalysts. *Micropor.Mesopor. Mater.* **2005**, *82*, 99–104.

(48) Giraud, F.; Geantet, C.; Guilhaume, N.; Loridant, S.; Gros, S.; Porcheron, L.; Kanniche, M.; Bianchi, D. Experimental Microkinetic Approach of De-NOx by NH_3 on $V_2O_5/WO_3/TiO_2$ Catalysts. 1. Individual Heats of Adsorption of Adsorbed NH_3 Species on a Sulfate-Free TiO_2 Support Using Adsorption Isobars. *J. Phys. Chem. C* **2014**, *118*, 15677−15692.

(49) Zecchina, A.; Marchese, L.; Bordiga, S.; Pazè, C.; Gianotti, E. Vibrational Spectroscopy of NH_4^+ Ions in Zeolitic Materials: An IR Study. *J. Phys. Chem. B* **1997**, *101*, 10128–10135.

(50) Plaza, I.; Rubin, J.; Laguna, M.A.; Bartolomé, J. Optical spectroscopy of the NH_4^+ internal vibrations in the orthorhombic phase of NH_4MF_3 (M is Mn, Zn) perovskites. *Spectrochimica Acta Part A* **1996**, *52*, 57−67.

FIGURES CAPTIONS

Figure 1: *In situ* DRIFT spectra of BaOP at 380 °C under He, 30%H_2O-He and 30%D_2O-He. The background corresponds to the spectrum of dehydrated KBr.

Figure 2: Unit cell of the layered structure of the Brushite, containing Ca atoms (grey), O atoms (red), H atoms (yellow) and P atoms (green).

Figure 3: Structures of the (010) surface of $CaHPO_4 \cdot nH_2O$ with different water coverages, θ (H_2O)=1 ML, 7/8 ML, 1/8 ML and 0 ML. Only half of the surface structure is shown here for simplicity. The two different types of water molecules are marked as W_a and W_b highlighted by a black circle in the top left structure, which corresponds to the structure obtained as cleaved from the bulk. The H bond network of W_a and W_b is shown in light blue dashed lines. At 1ML, 8 water molecules are found. At 7/8ML, one W_b water has been removed and the black circle indicates its former position. At 1/8ML, only one water molecule remains (W_a type) as highlighted by a black circle. Color-coding: grey for calcium, red for oxygen, green for phosphorus and yellow for hydrogen.

Figure 4: Surface energy in eV/Å^2 of Brushite (010) surfaces with various coverages (θ(H_2O)=1 ML, 7/8 ML, 1/8 ML and 0 ML) in water as function of the temperature and under a pressure in water of 1 atm.

Figure 5: Computed structure of the defective surface. The Ca^{2+} vacancy is shown with a blue circle, the H_{down} with a pink dashed circle and H_{up} with a pink solid circle. The calculated wavenumbers (after rescaling as mentioned in the 2.3 section) of ν(PO-H) vibrations on the first layer are also shown nearby in cm^{-1}. Color-coding: grey for calcium, red for oxygen, green for phosphorus and yellow for hydrogen, except surface Hup, which is marked in white.

Figure 6: Evolution of the FTIR spectra of BaOP after adsorption of lutidine and desorption under vacuum at increasing temperature.

Figure 7: Evolution of the IR bands of NH_3 adsorbed species on pre-treated BaOP catalyst recorded under 2%NH_3-He flow from 120 to 7 °C. The backgrounds correspond to the spectra recorded after pretreatment under He flow at the same temperatures, mass of the pellet 53 mg.

Figure 8: Structures (top view) and computed wavenumbers (in cm^{-1}) of the ν(PO-H) stretching vibrations and of the NH_3 or NH_4^+ vibrations after the adsorption of NH_3 on the non-defective dehydrated surface (A and B) and on the defective surface (C and D) at a coverage of $\theta(NH_3)=1/4$ ML. The corresponding adsorption energies are reported in Table 2. Color-coding: grey for calcium, red for oxygen, green for phosphorus, blue for nitrogen and yellow for hydrogen, except surface H_{up}, which is marked in white.

Figure 9: Evolution of the IR bands of NH_3 adsorbed species on pre-treated BaOP catalyst recorded under 1%NH_3-3%H_2O-He flow from 172 to 28 °C. The backgrounds correspond to the spectra recorded after pretreatment under He flow at the same temperatures, mass of the pellet 53 mg.

Figure 10: Structures and computed wavenumbers (in cm-1) of the ν(PO-H) stretching vibrations, water vibration and of the NH_3 or NH_4^+ vibration after the adsorption of NH_3 on the non-defective dehydrated surface (E and F) and on the defective surface (G). The corresponding adsorption energies are reported in Table 2. Color-coding: grey for calcium, red for oxygen, green for phosphorus, blue for nitrogen and yellow for hydrogen, except surface H_{up}, which is marked in white.

TABLES CAPTIONS

Table 1: Influence of the PO-H orientation in the non-defective dehydrated (010) surface of Brushite on the stability at 380 °C and the computed wavenumbers of ν(PO-H), reported after rescaling as mentioned in the 2.3 section.

Table 2: Adsorption energy of water and ammonia on the non-defective and defective surface corresponding to the structures shown in Figure 8 and Figure 10. The adsorption of ammonia is given as a successive adsorption after the adsorption of water on structures E, F and G.

TOC Graphic

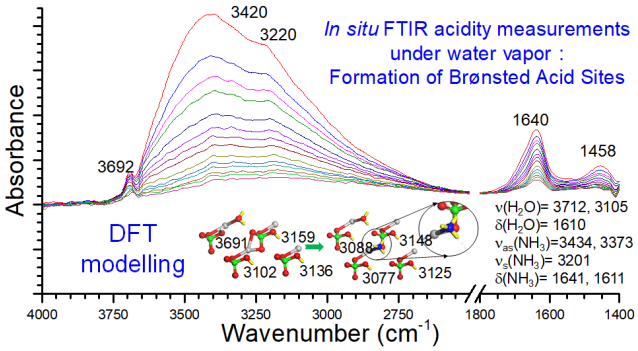
3420
3220
In situ FTIR acidity measurements
under water vapor :
Formation of Brønsted Acid Sites
1640
1458
3692
Absorbance
DFT
modelling
3691
3159
3102
3136
3088
3148
3077
3125
ν(H2O)= 3712, 3105
δ(H2O)= 1610
νas(NH3)=3434, 3373
νs(NH3)= 3201
δ(NH3)= 1641, 1611
4000
3750
3500
3250
3000
2750
1800
1600
1400
Wavenumber (cm-1)

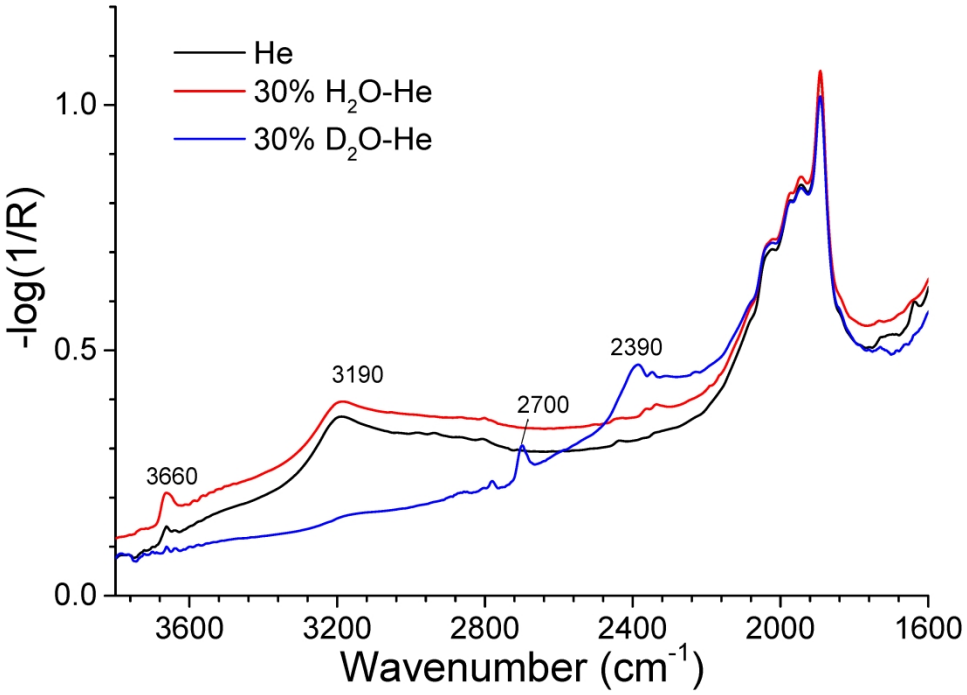

Figure1

297x210mm (300 x 300 DPI)

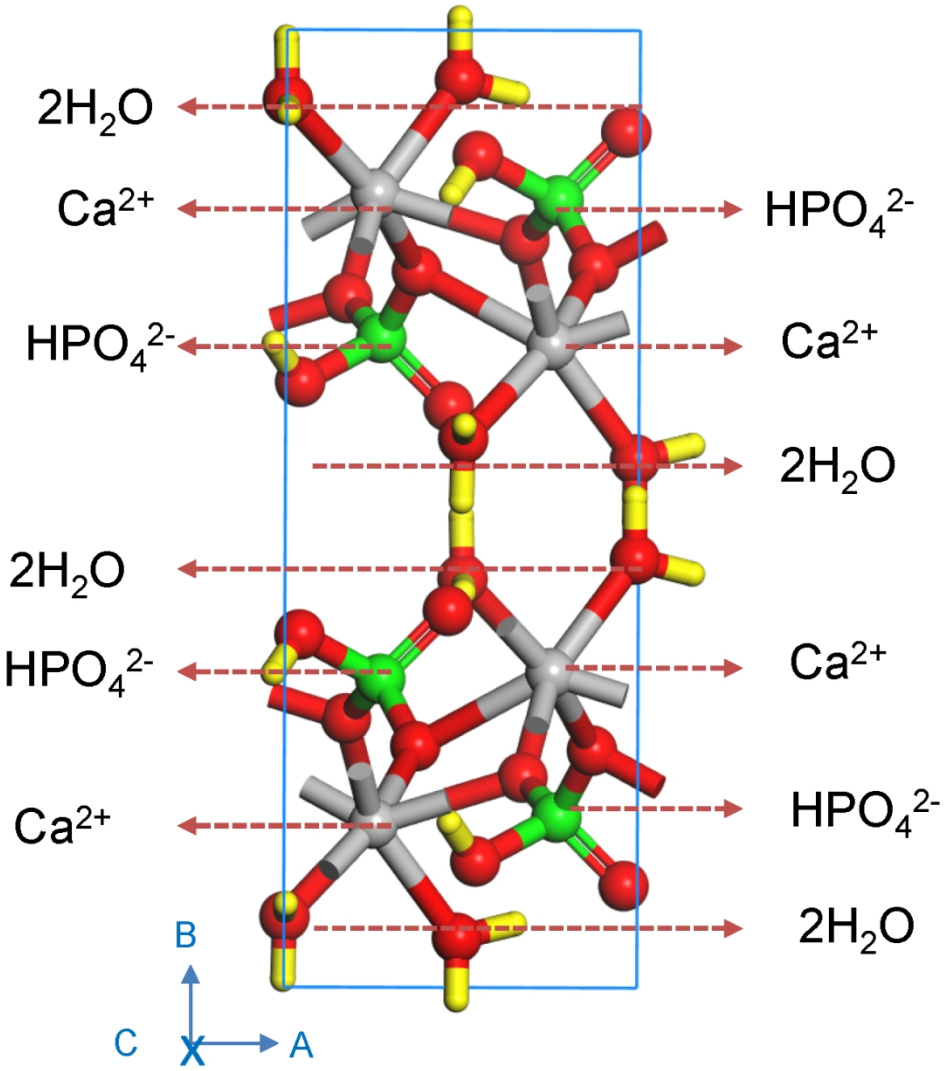

Figure2

117x132mm (300 x 300 DPI)

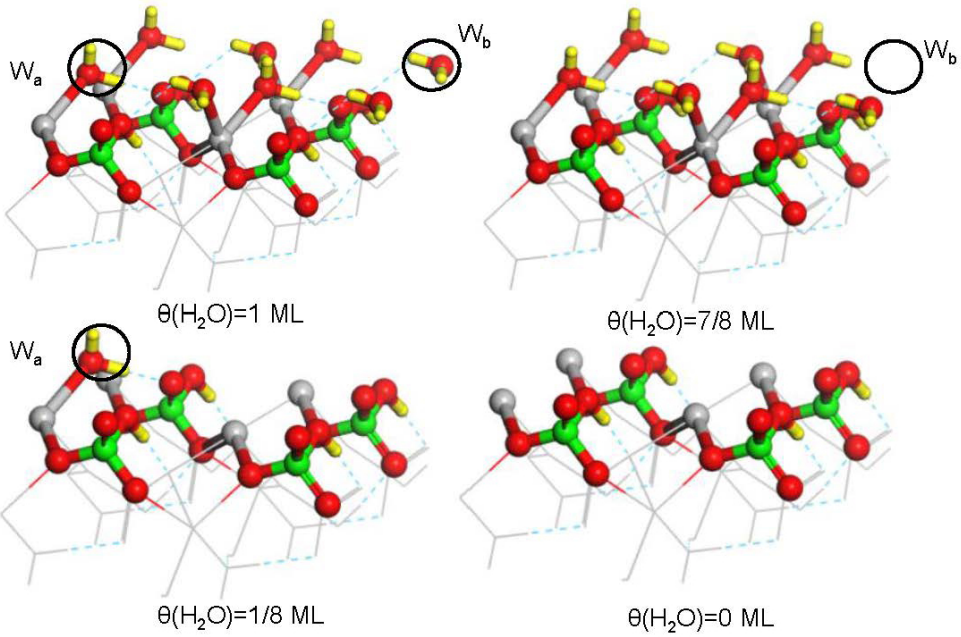

Figure 3

199x132mm (142 x 142 DPI)

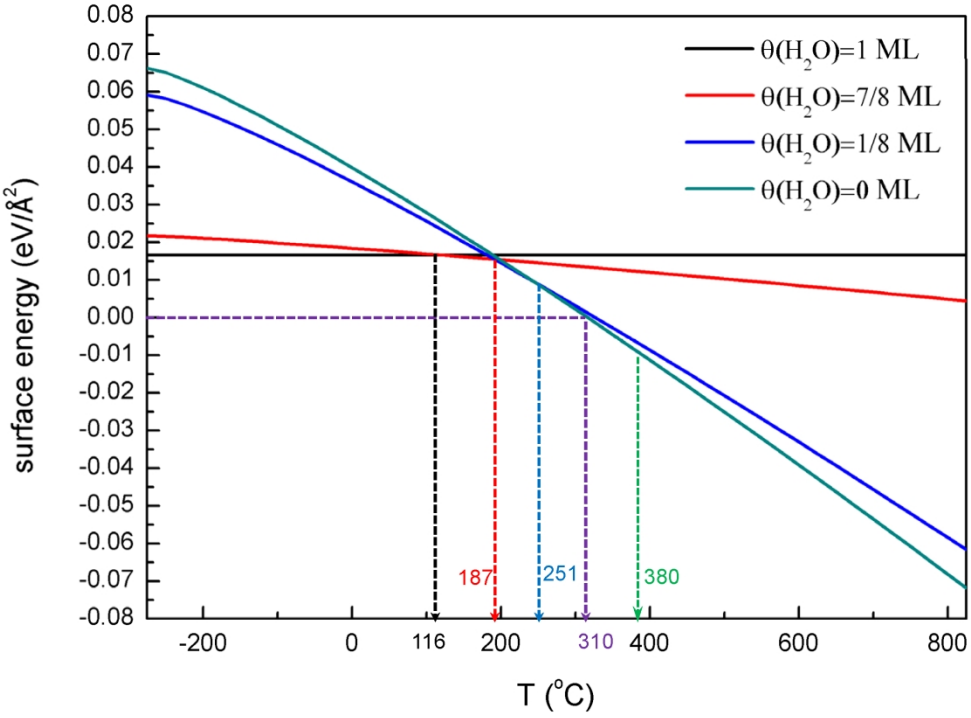

Figure4

226x165mm (300 x 300 DPI)

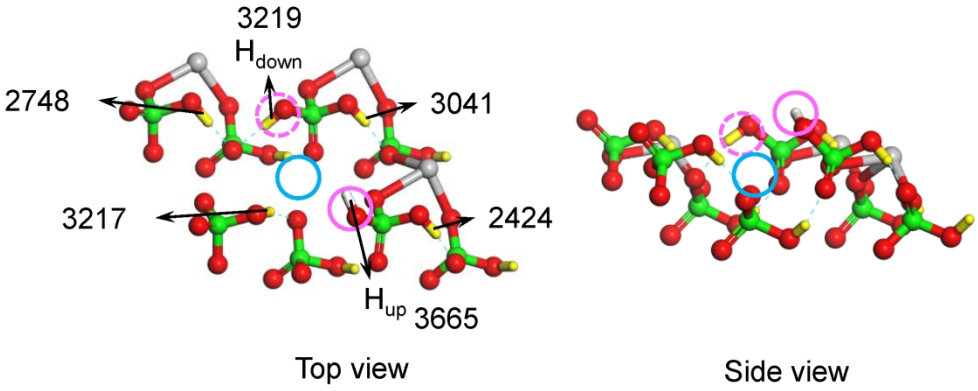

Figure5

192x78mm (300 x 300 DPI)

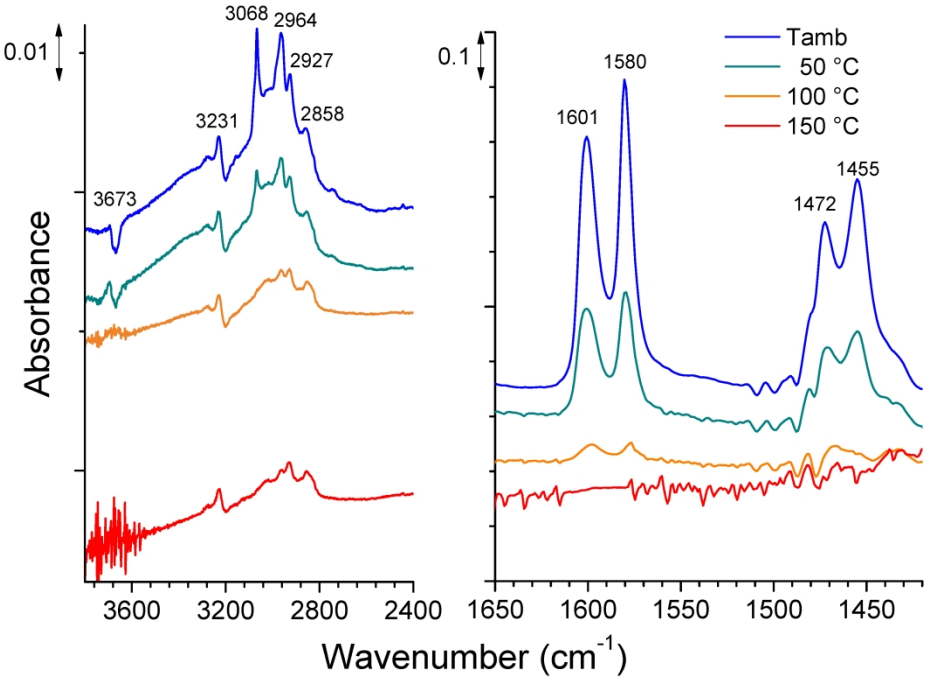

Figure6

297x210mm (300 x 300 DPI)

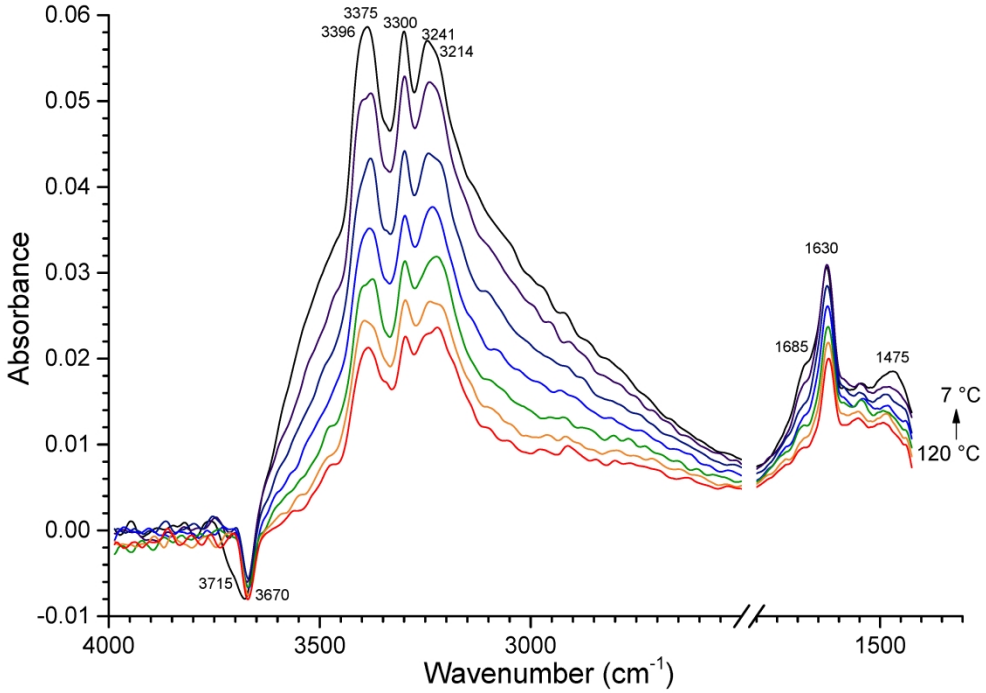

Figure7

297x210mm (300 x 300 DPI)

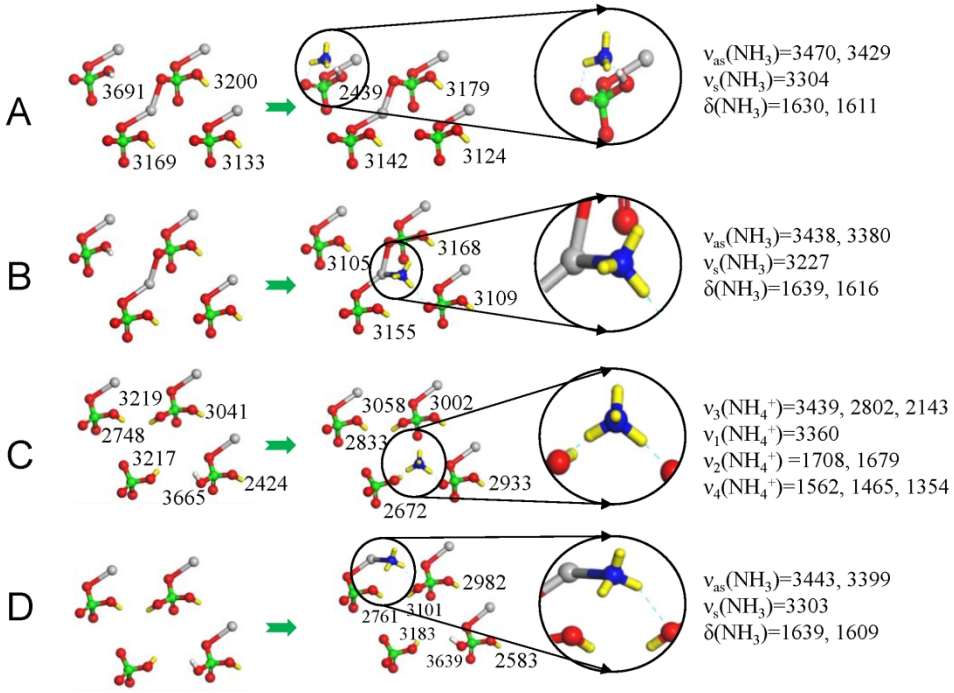

Figure8

191x135mm (300 x 300 DPI)

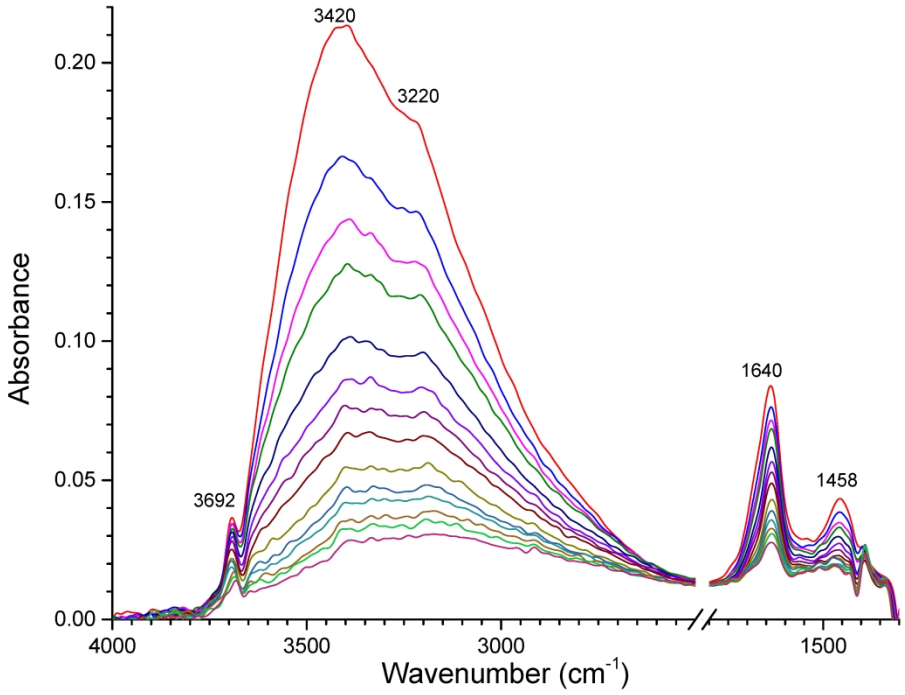

Figure9

297x210mm (300 x 300 DPI)

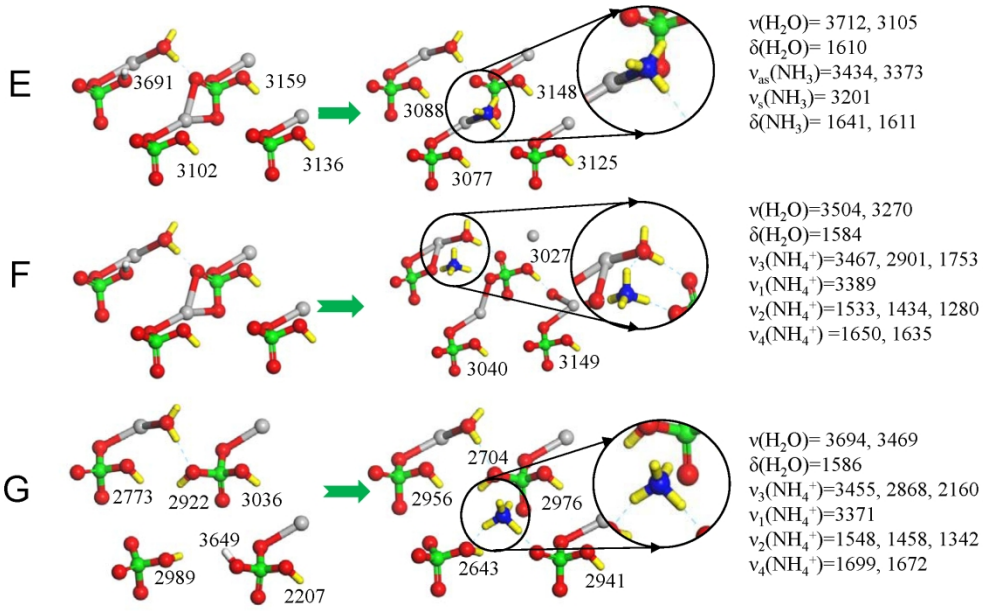

Figure10

204x129mm (300 x 300 DPI)

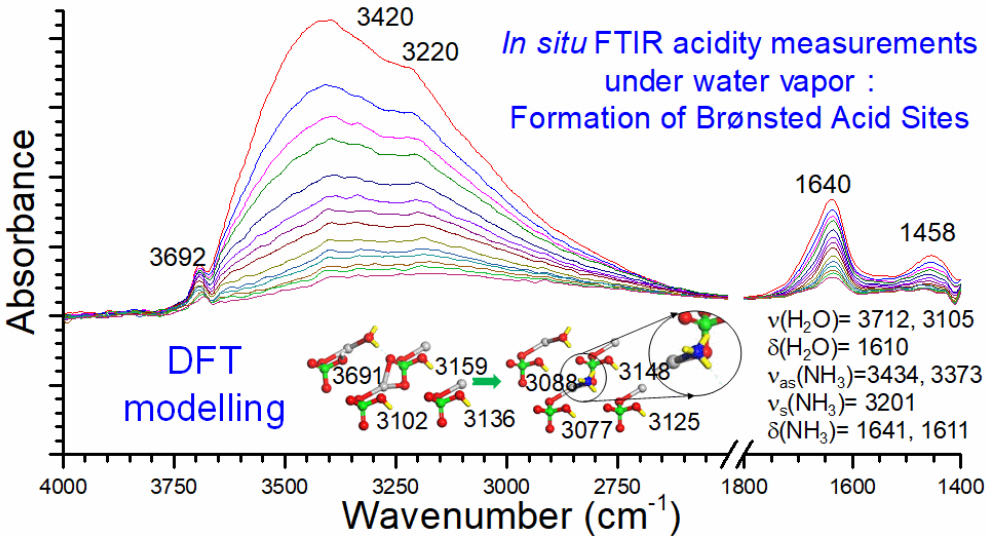

TOC Graphic

82x44mm (300 x 300 DPI)